

Topological Autoencoders++: Fast and Accurate Cycle-Aware Dimensionality Reduction

Mattéo Clémot, Julie Digne, Julien Tierny

Abstract—This paper presents a novel topology-aware dimensionality reduction approach aiming at accurately visualizing the cyclic patterns present in high dimensional data. To that end, we build on the *Topological Autoencoders* (TopoAE) [1] formulation. First, we provide a novel theoretical analysis of its associated loss and show that a zero loss indeed induces identical persistence pairs (in high and low dimensions) for the 0-dimensional persistent homology (PH^0) of the Rips filtration. We also provide a counter example showing that this property no longer holds for a naive extension of TopoAE to PH^d for $d \geq 1$. Based on this observation, we introduce a novel generalization of TopoAE to 1-dimensional persistent homology (PH^1), called TopoAE++, for the accurate generation of cycle-aware planar embeddings, addressing the above failure case. This generalization is based on the notion of *cascade distortion*, a new penalty term favoring an isometric embedding of the 2-chains filling persistent 1-cycles, hence resulting in more faithful geometrical reconstructions of the 1-cycles in the plane. We further introduce a novel, fast algorithm for the exact computation of PH for Rips filtrations in the plane, yielding improved runtimes over previously documented topology-aware methods. Our method also achieves a better balance between the topological accuracy, as measured by the Wasserstein distance, and the visual preservation of the cycles in low dimensions. Our C++ implementation is available at <https://github.com/MClemot/TopologicalAutoencodersPlusPlus>.

Index Terms—Topological data analysis, persistent homology, dimensionality reduction.

I. INTRODUCTION

DIMENSIONALITY reduction (DR) [9], [10] is a fundamental tool in data science for apprehending high-dimensional data. Such datasets are typically represented as a set of n points $X = \{x_0, x_1, \dots, x_{n-1}\}$ living in a high-dimensional Euclidean space \mathbb{R}^h . Then, the goal of DR is to compute an embedding $Z = \phi(X)$ of this input point cloud in a lower-dimensional Euclidean space \mathbb{R}^ℓ , with $\ell \ll h$. This process can be motivated in practice by the need to either (i) simplify the input data (to facilitate further processing and analysis) or to (ii) generate a visualization of the data that can be interpreted by a human observer (e.g., $\ell = 2$ yields planar views of the input point cloud).

Unless X is already *flat* (e.g., living in an ℓ -dimensional hyperplane), its projection to \mathbb{R}^ℓ will necessarily involve a form of *distortion*. Depending on the application needs, several distortion criteria have been introduced in the literature. Then, a vast corpus of DR algorithms [11]–[13] have been proposed,

Mattéo Clémot is with University Claude Bernard Lyon 1. E-mail: matteo.clemot@univ-lyon1.fr

Julie Digne is with the CNRS and University Claude Bernard Lyon 1. E-mail: julie.digne@cnrs.fr

Julien Tierny is with the CNRS and Sorbonne University. E-mail: julien.tierny@sorbonne-universite.fr

either (i) to minimize a specific distortion criterion, or (ii) to preserve interesting geometrical features (thereby indirectly minimizing the associated distortion criterion). For instance, the seminal multidimensional scaling algorithm [10] aims at minimizing metric distortion, which is achieved in practice by trying to preserve pairwise distances.

In many use-cases, it may be desirable to preserve *topological* characteristics when projecting down to a visual space. For instance, the preservation of the *clusters* present in high-dimensions enables a quick visual interpretation of the main trends in the dataset. *TopoMap* [7], for example, guarantees that, after its projection, the hierarchical clustering of the dataset is identical in high and low dimensions. This provides users with strong confidence regarding the structural interpretation of the projected data. Technically, the preservation of hierarchical clusters relates to the preservation of the 0-dimensional persistent homology (PH^0) of the Rips filtration of X (see Sec. III-B for a technical description). In this context, several topology-aware DR methods [1], [7], [14] have been proposed, but these mostly focused in practice on preserving PH^0 , i.e., the data point clusters (see Sec. II-B).

In this work, we investigate the preservation of more advanced topological features than clusters. In particular, we focus on the preservation of the cyclic structures, the *topological handles* captured by PH^1 , when projecting to a planar visual space (i.e., $\ell = 2$). Some datasets indeed include a periodic nature (e.g., time-series), yielding cycles in the high-dimensional space. Then, preserving these cyclic patterns in the visualization is important to visually convey and characterize the periodicity of the studied phenomenon. Examples of such datasets are provided in Sec. VII-A, with the *MoCap* dataset capturing a recurring periodic gesture or with the *SingleCell* dataset, capturing gene expression at different stages of the cell life cycle.

However, preserving PH^1 while projecting to the plane is a significantly more challenging problem than preserving PH^0 . First, from a computational point of view, the 0-dimensional case is a very specific instance of PH computation, which can be efficiently computed with a union-find data structure [15] (with a runtime complexity that is virtually linear with the number of considered edges in the Rips complex). As of dimension 1, generic PH computation algorithms need to be considered, with a worst case runtime complexity that is cubic with the number of considered simplices. Second, as discussed by several authors [1], [7], PH^0 preservation can be obtained by finding a planar layout of X which preserves its minimum spanning tree (MST). Since trees can always be embedded in the plane, the existence of (at least) one

Input	Global methods		Locally topology-aware methods			Globally topology-aware methods			TopoAE++
	PCA [2]	MDS [3]	Isomap [4]	t-SNE [5]	UMAP [6]	TopoMap [7]	TopoAE [1]	TopoAE+ \mathcal{W}^1 [8]	
3Clusters ($n = 800$)									
	4.5e-01	5.0e-01	4.7e-01	2.3e+01	7.2e-01	4.3e+00	5.8e-01	1.1e-01	<u>4.4e-01</u>
	<u>2.7e-01</u>	<u>4.1e-01</u>	1.1e+00	3.5e+01	8.5e+00	7.0e+00	1.3e+00	1.5e+00	6.4e-01
	0.00049	2.5	0.16	0.76	2.6	0.086	81	830	5.0
Twist ($n = 100$)									
	1.1e+00	2.2e-01	1.9e+01	3.3e+00	1.5e+01	1.8e-01	1.6e-01	1.8e-05	<u>1.7e-03</u>
	<u>2.2e-01</u>	<u>2.1e-01</u>	2.4e+00	3.9e+00	2.8e+00	8.2e-01	3.8e-01	7.3e-01	7.8e-01
	0.00049	0.073	0.0072	0.20	2.3	0.74	2.2	6.3	2.5
K_4 ($n = 300$)									
	2.7e-01	2.8e-01	3.8e-01	4.7e+01	3.9e-01	1.4e-01	6.5e-02	7.9e-04	<u>2.4e-02</u>
	<u>2.7e-01</u>	<u>1.8e-01</u>	5.1e-01	1.6e+01	9.1e+00	5.7e-01	1.0e+00	6.8e-01	3.4e-01
	0.00048	0.22	0.026	0.46	2.4	1.7	11	63	6.2

Fig. 1. Comparison of DR methods on three synthetic 3D point clouds (see Sec. VII-A for a description), along with the metric distortion $\mathfrak{D}(X, Z)$ between the input X and its planar embedding Z , the Wasserstein distance $\text{PDW}^1(X, Z) = \mathcal{W}_2(\mathcal{D}_{\text{Rips}}^1(X), \mathcal{D}_{\text{Rips}}^1(Z))$ between their respective 1-dimensional persistence diagrams, and the running time t in seconds. The best value for an indicator is written in bold, the second best is underlined. In the second line, a generator of the most persistent PH^1 pair in the high-dimensional input is projected in the 2D embedding in transparency and slightly smoothed for visualization purposes (to distinguish it from the point cloud). The generator color map depicts its arc-length parameterization. In the third line, the input – that is sampled around the edges of a tetrahedron in 3D – features 3 significantly persistent PH^1 pairs, and a generator for each is represented both in the input and in the 2D embeddings with a specific color. Quantitatively, our approach (TopoAE++) generates planar embeddings with competitive Wasserstein distances. Qualitatively, it produces planar embeddings yielding less crossings of the projected high-dimensional persistent generators (colored curves), thereby producing visualizations that depict more faithfully the topological handles present in high dimensions.

solution (i.e., a projection preserving PH^0) is guaranteed. Unfortunately, this observation no longer holds for higher dimensional PH. As discussed later in Sec. VII-D, it is easy to design examples of high-dimensional point clouds whose PH^1 cannot be preserved through planar projections (e.g., a dense sampling of a non-planar graph, see Fig. 13). The existence of such cases, for which an exact preservation of PH^1 cannot be obtained, illustrates the difficulty of the problem, and the need for efficient optimization methods for preserving PH^1 as accurately as possible, which is the topic of this paper.

Specifically, this paper revisits the *Topological Autoencoders* (TopoAE), a prominent technique in topology-aware dimensionality reduction, which we extend into TopoAE++, for the accurate visualization of the cyclic patterns present in the data. We make the following new contributions:

- 1) *A novel theoretical analysis of TopoAE’s loss ($\mathcal{L}_{\text{TAE}}^0$):*
 - We show that $\mathcal{L}_{\text{TAE}}^0$ is an upper bound of the Wasserstein distance between the 0-dimensional persistence diagrams in high and low dimensions, with regard to the Rips filtration. In particular, when $\mathcal{L}_{\text{TAE}}^0 = 0$, the persistence pairs are identical in high and low dimensions for the 0-dimensional persistent homology (PH^0) of the Rips filtration.
 - We provide a counter example showing that the above property does not hold for a naive extension of TopoAE to 1-dimensional persistent homology (PH^1), with a loss noted $\mathcal{L}_{\text{TAE}}^1$.
- 2) *A generalization of TopoAE’s loss for 1-dimensional persistent homology (PH^1):* We introduce a new loss called *cascade distortion* (CD), noted $\mathcal{L}_{\text{CD}}^1$, which addresses the above counter example. This term favors an isometric

embedding of the 2-chains filling persistent 1-cycles. We show that for PH^0 this loss generalizes TopoAE’s loss (i.e., $\mathcal{L}_{\text{CD}}^0 = \mathcal{L}_{\text{TAE}}^0$). Extensive experiments show the practical performance of this loss for the accurate preservation of generators through the projection.

- 3) *An efficient computation algorithm for TopoAE++:* To accelerate runtime, we provide a new, fast algorithm for the exact computation of PH for Rips filtrations in the plane. This geometric algorithm relies on the fast identification of cycle-killing triangles via local minmax triangulations of the relative neighborhood graph, leveraging duality for the efficient computation of PH^1 . We believe this contribution to be of independent interest.
- 4) *Implementation:* We provide a C++ implementation of our algorithms that can be used for reproducibility.

II. RELATED WORK

The literature related to our work can be classified into two categories: general purpose DR techniques (Sec. II-A) and topology-aware techniques (Sec. II-B).

A. General purpose dimensionality reduction

Numerous DR techniques have been proposed and the related literature has been summarized in several books [9], [10] and surveys [11]–[13]. Principal Component Analysis (PCA) [2] is by far the most popular linear DR technique. Although it is an indispensable tool for data analysis, its linear nature does not always allow it to apprehend complex non-linear phenomena. One of the first non linear DR methods is the multidimensional scaling (MDS) [3]. It aims at preserving

as far as possible the pairwise distances in the high- and low-dimensional point clouds. Another approach, particularly related to our work, consists in optimizing an autoencoder neural network [16]. The *encoder* is used to represent the explicit projection map from the high-dimensional input space to the low-dimensional representation space, while the *decoder* tries to reconstruct the input data from its encoded representation. We will refer to these methods as *global* methods.

Global methods have been used successfully in many applications, but they do not take into account the possible distribution of the input points over some implicit, unknown manifold. This may lead to the unwanted preservation of distances between points that are close in the ambient space but far apart on this manifold. *Locally topology-aware* methods have therefore been introduced to address this issue. For instance, Isomap [4] preserves geodesic distances on a captured manifold structure of the input data. Other methods also feature neighborhood preservation objectives. For example, Local Linear Embedding (LLE) [17] relies on linear reconstructions of local neighborhoods. Other methods leverage additional landmarks [18] or user-provided control points [19].

All these methods try to preserve local Euclidean distances when projecting to a lower dimension. However, this can sometimes lack relevance in the applications, especially with high-dimensional datasets for which the distribution of pairwise Euclidean distances tend to be uniform. For such cases, local distance preservation fails at characterizing well relevant local relations. To alleviate this issue, SNE [20] and later t-SNE [5] use a conditional probability formulation to represent similarities between points and try to have similar distributions both in high- and low-dimension thanks to a Kullback–Leibler divergence minimization. More recently UMAP has been introduced [6] along a theoretical foundation on category theory. It provides results that are similar visually to t-SNE, but in a more scalable way. Variants were later introduced to better preserve the global structure in the embedding, such as TriMAP [21] that constrains the proximity order within triplets of points, or PaCMAP [22] that adds constraints on more distant point pairs. Although these methods succeed in preserving the local topology, they are not explicitly aware of the global structure of the input, which can lead to the loss of noteworthy global, topological features.

B. Globally topology-aware dimensionality reduction

Topology-based methods have become popular over the last two decades in data analysis and visualization [23] and have been applied to various areas: astrophysics [24], [25], biological imaging [26]–[28], quantum chemistry [29]–[31], fluid dynamics [32], [33], material sciences [34]–[36], turbulent combustion [37], [38]. They leverage tools that define concise signatures of the data based on its topological properties and that have been summarized in topological data analysis reference books [39], [40] and surveys [41].

Several DR methods have been proposed by the visualization community to preserve specific topological signatures of the input data. For instance, terrain metaphors have been investigated for the visualization of an input high-dimensional

scalar field, in the form of a three-dimensional terrain, whose elevation yields an identical contour tree [42] or an identical set of separatrices [43], [44]. This framework has been extended to density estimators [45]–[48] for the support of high-dimensional point clouds. However, such metaphors completely discard the metric information of the input space [45], possibly placing next to each other points which are arbitrarily far in the input space (and reciprocally). Yan et al. [49] introduced a DR approach driven by the Mapper structure [50], an approximation of the Reeb graph [51], which can capture in practice large handles in the data, however without guarantees, since the number of handles in the considered manifold is only an upper bound on the number of loops in the Reeb graph [39].

To incorporate the metric information from the input data while preserving at the same time some of their topological characteristics, several approaches have focused on driving the projection by the *persistence diagram* of the Rips filtration of the point cloud (see Sec. III-B for a technical description). Carriere et al. [8] presented a generic persistence optimization framework with an application to dimensionality reduction. Their approach explicitly minimizes the Wasserstein distance (Sec. III-B) between the 1-dimensional persistence diagrams in high and low dimensions. However, this approach solely focuses on this penalization term. As a result, although the number and persistence of cycles may be well-preserved, the solver tends to produce cycles in low dimensions which involve arbitrary points (e.g., which were not necessarily located along the cycles in high dimensions), which challenges visual interpretation, as later detailed in Sec. VII-D.

To enforce a correspondence between the topological features at the data point level, additional structures need to be preserved. For the specific case of 0-dimensional persistent homology (PH^0), Doraiswamy et al. introduced *TopoMap* [7], an algorithm which constructively preserves the *persistence pairs* (Sec. III-B) through the preservation of the minimum spanning tree of the data. An accelerated version, with improved layouts, has recently been proposed [52]. Alternative approaches have considered the usage of an optimization framework (typically based on an autoencoder neural network [16]), with the integration of specific topology-aware losses [1], [14], [53]–[55]. Among them, a prominent approach is the *Topological Autoencoders* (TopoAE) [1]. Its loss aims at preserving the diameter of the simplices involved in persistence pairs, when going from high to low dimensions and reciprocally. However, the above techniques focused in practice on the preservation of PH^0 and did not, to our knowledge, report experiments regarding the preservation of higher dimensional PH. Specifically, we show in Sec. IV that, while a zero TopoAE loss indeed implies a preservation of the persistence pairs for PH^0 , it is not the case for higher dimensional PH. We provide a counter example for PH^1 , which is addressed by our novel, generalized loss.

III. BACKGROUND

This section presents the technical background to our work. We refer the reader to textbooks [39], [40] for comprehensive introductions to computational topology.

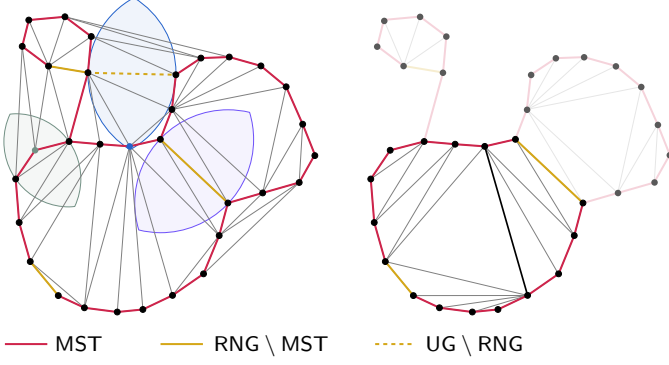


Fig. 2. Left: geometric graphs for a point cloud X in the plane. Its MST is depicted in red. The edges from the RNG which are not in the MST are shown in continuous yellow, while those which are in the UG but not in the RNG are shown in dashed yellow. The remaining Delaunay edges are shown in gray. Three lenses are shown: the purple one is devoid of points of X , therefore the associated yellow edge belongs to the RNG; the blue one – associated with the dashed yellow edge – is devoid of points of the link of that edge but contains another point of X (the blue one), therefore this edge is in the UG but not in the RNG; the green one contains the green point and the associated gray edge is not in RNG nor in UG. Right: within the highlighted bottom RNG-polygon, a MML triangulation has replaced the Delaunay triangulation, with its longest edge highlighted in black. Note that for the two other polygons, the Delaunay triangulation is already a MML triangulation within these polygons.

A. Geometric structures

We introduce below geometric concepts related to persistent homology (Sec. III-D) that are relevant to our algorithm.

We consider in this section a point cloud X containing n points, in a d -dimensional space \mathbb{R}^d endowed with the ambient Euclidean metric. The lens of an edge $(a, b) \in X^2$ is defined as the points of X whose distance to either a or b is smaller than $\|a - b\|_2$. The relative neighborhood graph $\text{RNG}(X)$ [56] is the graph on X that features every edge with an empty lens, i.e., $\text{RNG}(X) = \{e \in X^2 \mid \text{Lens}(e) = \emptyset\}$. The RNG is known to be a subset of the Delaunay triangulation [56]. In the plane, it can be computed in time $\mathcal{O}(n \log n)$ [57]–[59]. The Urquhart graph $\text{UG}(X)$ [60] is another subgraph of the Delaunay triangulation that is obtained by removing the longest edge of each triangle. It can also be thought as the subgraph of $\text{DEL}(X)$ that only keeps edges whose lens does not contain any points of its link¹. Finally, we write $\text{MST}(X)$ the Euclidean minimum spanning tree of X , i.e., the tree spanning X that minimizes the sum of the Euclidean distances of its edges. Under general position hypothesis², we have the following inclusions [56] (Fig. 2, left, shows a case where the three inclusions are strict):

$$\text{MST}(X) \subseteq \text{RNG}(X) \subseteq \text{UG}(X) \subseteq \text{DEL}(X). \quad (1)$$

Our algorithm also relies on the minmax length (MML) triangulations of a planar point cloud $X \subset \mathbb{R}^2$. It is defined as a triangulation that minimizes the length of its longest

¹In an abstract simplicial complex \mathcal{K} (i.e., a family of sets that is closed under taking subsets, where sets represent simplices and their subsets represent their faces), the link of a simplex $\sigma \in \mathcal{K}$ is the set $\{\tau \in \mathcal{K} \mid \sigma \cap \tau = \emptyset \text{ and } \sigma \cup \tau \in \mathcal{K}\}$. It provides a notion of neighborhood boundary for σ .

²i.e., we suppose that no $d+2$ points lie on a common $(d-1)$ -sphere (for the Delaunay triangulation [39]), and that pairwise distances are unique for the uniqueness of the MST, which can be enforced via small perturbations.

edge (Fig. 2, right). Such a triangulation can be computed in quadratic time $\mathcal{O}(n^2)$ with an algorithm [61] that breaks down the construction of such a triangulation over each polygon formed by the RNG and the convex hull of X .

We conclude this section with a geometric construction that is often used in the topological data analysis of point clouds: the Rips complex of X with diameter threshold $r \geq 0$ is the simplicial complex featuring all the simplices $\sigma \subset X$ whose diameter $\delta(\sigma) = \max_{x, y \in \sigma} \|x - y\|_2$ is smaller than r (i.e., every edge included in σ must be shorter than r) (see Fig. 3):

$$\text{Rips}_r(X) = \{\sigma \subset X \mid \delta(\sigma) \leq r\}. \quad (2)$$

We write $\mathcal{K}^k = \{\sigma \in \mathcal{K} \mid \dim \sigma = k\}$ the set of k -simplices of a simplicial complex \mathcal{K} , and $\mathcal{K}^{(k)} = \{\sigma \in \mathcal{K} \mid \dim \sigma \leq k\}$ its k -skeleton. Then, $\text{Rips}_r^{(k)}(X)$ is the Rips complex of X with diameter $r \geq 0$ and maximum simplex dimension k .

B. Persistent homology

Persistent homology, introduced independently by several authors [62]–[65], focuses on the evolution of the topological properties of an increasing sequence of m nested simplicial complexes $\mathbb{K} = (\mathcal{K}_0, \mathcal{K}_1, \dots, \mathcal{K}_{m-1})$, which is called a *filtration*. Persistent homology can be applied on various filtrations, like the sublevel sets of a scalar field on a mesh. However a filtration of particular interest for point clouds is the Rips filtration (Fig. 3), which consists in the sequence of Rips complexes with an increasing threshold r . More precisely, the Rips filtration of X can be written as $(\text{Rips}_0(X), \text{Rips}_{r_1}(X), \dots, \text{Rips}_{r_{m-1}}(X), \text{Rips}_\infty(X))$ with increasing r_i 's such that the Rips complex changes between r_i and r_{i+1} (i.e. $\text{Rips}_{r_i}(X) \subsetneq \text{Rips}_{r_{i+1}}(X)$).

Persistent homology groups for a filtration \mathbb{K} are algebraic constructions that contain *persistent homology classes* and that are defined from homology groups (see Sec. A-A for a brief summary or [39] for a more complete introduction). Informally, these classes represent topological features (that can be geometrically interpreted as clusters for PH^0 , cycles for PH^1 , voids for the PH^2 ...) which appear at some point in the filtration and may disappear later. Formally, for $0 \leq i \leq j \leq m$, the k -th persistent homology group $\mathcal{H}_k^{i,j}(\mathbb{K})$ is the image of the k -th homology group $\mathcal{H}_k(\mathcal{K}_i)$ by the inclusion morphism $f_k^{i,j} : \mathcal{H}_k(\mathcal{K}_i) \rightarrow \mathcal{H}_k(\mathcal{K}_j)$. Its classes can be understood as those which already exist in $\mathcal{H}_k(\mathcal{K}_i)$ and that still exist in $\mathcal{H}_k(\mathcal{K}_j)$. Therefore, we say that a class $\gamma \in \mathcal{H}_k(\mathcal{K}_i)$ is *born* entering \mathcal{K}_i when $\gamma \notin \mathcal{H}_k^{i-1,i}(\mathbb{K})$, i.e., when it is not the image of a pre-existing class by the inclusion morphism. We also say that such a class born at \mathcal{K}_i *dies* entering \mathcal{K}_j when $f_k^{i,j-1}(\gamma) \notin \mathcal{H}_k^{i-1,j-1}(\mathbb{K})$ but $f_k^{i,j}(\gamma) \in \mathcal{H}_k^{i-1,j}(\mathbb{K})$, i.e., when γ is merged into a pre-existing class (possibly the 0 class) when going from \mathcal{K}_{j-1} to \mathcal{K}_j . In this case, the birth of γ is associated with a k -simplex $\sigma_i \in \mathcal{K}_i$ and its death with $(k+1)$ -simplex $\sigma_j \in \mathcal{K}_j$. Such a pair (σ_i, σ_j) is called a *persistence pair*. If the filtration is defined by scalar values f on the simplices (e.g., the diameter δ for the Rips filtration), the *persistence* of such a class is the positive value $f(\sigma_j) - f(\sigma_i)$.

In the specific case of a Rips filtration, we can say more simply that for any k , a PH^k pair of positive persistence

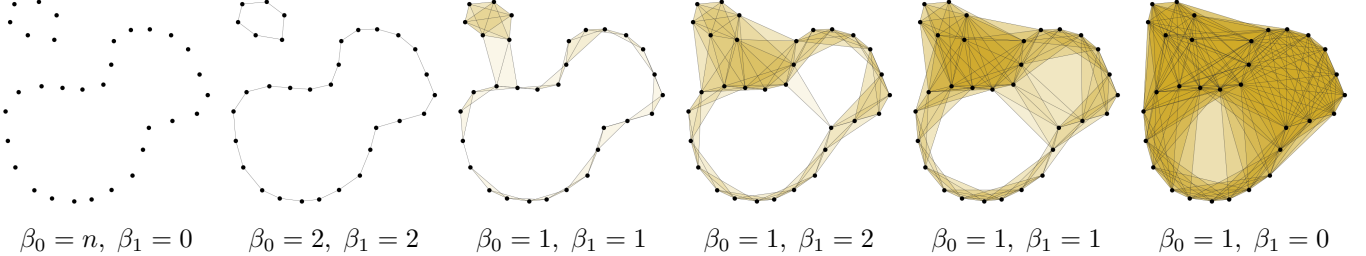


Fig. 3. Rips complexes of the same planar point cloud X , for increasing diameter thresholds r (only the 2-skeletons, i.e., the vertices, edges and triangles, of the simplicial complexes are shown). This threshold increase induces a sequence of nested simplicial complexes, whose topology varies along the process. From left to right, the number of connected components is successively n , then 2, then 1, while the number of handles is successively 0, 2, 1, 2, 1 and 0.

(σ_i, σ_j) is created (resp. killed) by the longest edge of σ_i (resp. σ_j). Indeed, a Rips complex is entirely determined by its 1-skeleton since the diameter of any simplex is the length of the longest edge it features (it is a *flag complex*). In the following we refer to these edges as *k-critical edges*.

Persistence diagrams (Fig. 4) are concise topological representations that summarize the persistent homology groups. More precisely, the k -th persistence diagram is a 2D multiset where each k -dimensional persistence pair (σ_i, σ_j) is represented by a point $(f(\sigma_i), f(\sigma_j)) \in \mathbb{R}^2$ above the diagonal. We write $\mathcal{D}^k(f)$ for the k -th persistence diagram of the filtration given by a scalar function $f : \mathcal{K} \rightarrow \mathbb{R}$, or directly $\mathcal{D}_{\text{Rips}}^k(X)$ for the k -th persistence diagram of the Rips filtration of X . Many point clouds have the same persistence diagrams: in particular, $\mathcal{D}_{\text{Rips}}^k(X)$ is invariant to point permutations in X .

Persistence diagrams (of equal homology dimension) are usually compared with metrics born of optimal transport that come with stability properties [66], [67]. Let $\mathcal{D}, \mathcal{D}' \subset \mathbb{R}^2$ be two persistence diagrams to be compared. We define the *augmented* diagrams as $\overline{\mathcal{D}} = \mathcal{D} \cup \Delta \mathcal{D}'$ and $\overline{\mathcal{D}'} = \mathcal{D}' \cup \Delta \mathcal{D}$ where Δ is the map that projects to the diagonal, i.e., $\Delta : (b, d) \mapsto (\frac{b+d}{2}, \frac{b+d}{2})$. This ensures that $|\overline{\mathcal{D}}| = |\overline{\mathcal{D}'}|$. The p -cost $c_p(x, y)$ between two points $x \in \overline{\mathcal{D}}$ and $y \in \overline{\mathcal{D}'}$ is defined as 0 if both x and y are on the diagonal and as \mathbb{R}^2 's p -norm $\|x - y\|_p$ otherwise. Then, the L_q -Wasserstein distance \mathcal{W}_q^p is:

$$\mathcal{W}_q^p(\mathcal{D}, \mathcal{D}') = \min_{\psi \in \Psi} \left(\sum_{x \in \overline{\mathcal{D}}} c_p(x, \psi(x)) \right)^{1/q}, \quad (3)$$

where $\Psi = \text{Bij}(\overline{\mathcal{D}}, \overline{\mathcal{D}'})$ (Fig. 4). Because for any fixed q , all \mathcal{W}_q^p are bi-Lipschitz equivalent [67], we focus on the distances $\mathcal{W}_p = \mathcal{W}_p^p$ with $p < \infty$. In practice, the Wasserstein distances \mathcal{W}_p can be approximated thanks to the *auction* algorithm, an asymmetric and generic approach introduced by Bertsekas [68] that can be specialized to persistence diagrams with dedicated data structures to leverage their geometric structure [69].

C. Persistence homology computation

Since the introduction of computational PH [65], numerous algorithms and implementations have been proposed, based either on the boundary matrix reduction approach or on its geometric interpretation known as the *PairCells* algorithm [40], which we detail in the following as our novel loss (introduced in Sec. V) is defined relatively to the *cascade*,

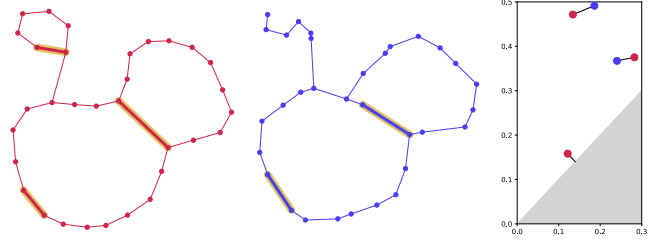


Fig. 4. Two point clouds (red and blue) in the plane represented with their RNG, along with their respective 1-dimensional persistence diagrams (right). The edges in $\text{RNG} \setminus \text{MST}$ are highlighted in bold and yellow. The number of non-diagonal points in each diagram is exactly the number of RNG-polygons in the associated point cloud (3 for the red one, 2 for the blue one), and also the number of $\text{RNG} \setminus \text{MST}$ edges. The optimal assignment inducing the Wasserstein distance \mathcal{W}_2 between them is shown in black.

an object computed by this algorithm. Indeed, *PairCells* computes not only persistent pairs but also representatives of each PH class for any simplicial complex \mathcal{K} with its simplices endowed with distinct scalar values $f(\sigma)$ that are increasing by inclusion (which induces the filtration of sublevel sets). For each k -simplex $\sigma \in \mathcal{K}$, it stores a k -chain $\text{cascade}(\sigma)$ that is initially equal to σ , and whose $(k-1)$ -boundary $\partial(\text{cascade}(\sigma))$ is, after the execution of the algorithm, a representative of the PH class killed by σ . In the following we will call this boundary a *persistent generator* of the PH class [70], [71]. In addition, these cascades will enable us in Sec. V to find 2-chains that fill the 1-cycles.

PairCells (Alg. 1) takes one k -simplex $\sigma \in \mathcal{K}$ at a time, by increasing value $f(\sigma)$, and applies the *EliminateBoundaries* procedure (Alg. 2) on it. This procedure runs a *homologous propagation* [71] from σ : the $(k-1)$ -boundary $\partial(\text{cascade}(\sigma))$ is expanded step by step, each time selecting its *youngest* $(k-1)$ -simplex τ (i.e., the one with the highest value $f(\tau)$) and adding modulo 2 to $\text{cascade}(\sigma)$ the cascade associated with the partner of τ , if it exists (see Fig. 5). The procedure stops either when an unpaired simplex τ is selected, in which case σ and τ are paired together since σ kills the $(k-1)$ -dimensional homology class introduced by τ ; or when the boundary $\partial(\text{cascade}(\sigma))$ becomes empty, in which case we know that σ creates a k -dimensional homology class. This algorithm can be understood as a geometric interpretation of the persistence algorithms based on boundary matrix reduction.

In practice, if we are not interested in the cascades them-

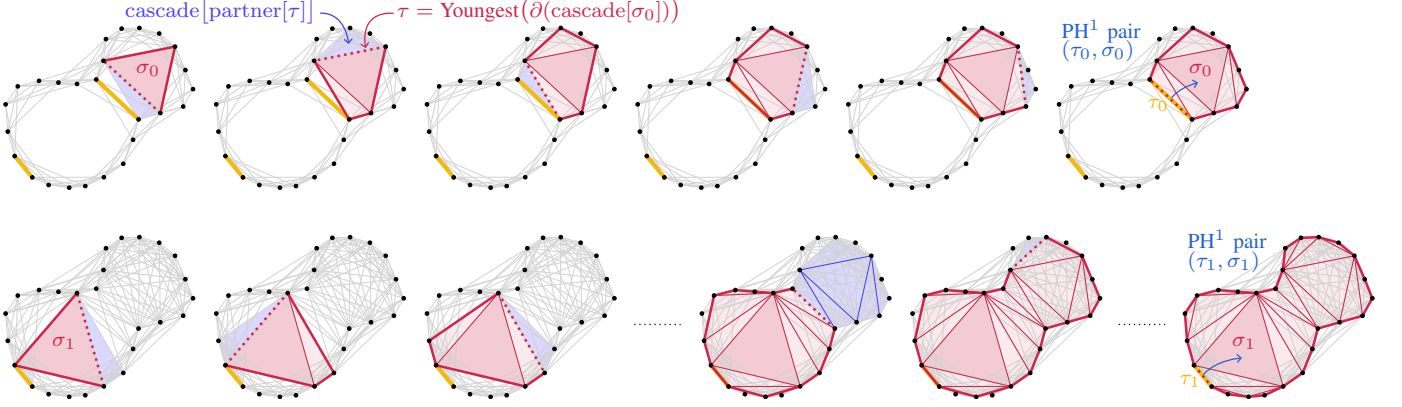


Fig. 5. Some steps of two executions of the `EliminateBoundaries` Alg. 2 procedure run on the 2-simplices σ_0 (top line) and σ_1 (bottom line), corresponding to the creation of two PH^1 pairs in the previous planar point cloud (with its smallest cycle removed for clarity). Unpaired edges – which are in $\text{RNG}(X) \setminus \text{MST}(X)$ – are depicted in yellow. At each step, $\text{cascade}[\sigma]$ is shown in red, and its boundary $\partial(\text{cascade}[\sigma])$ is highlighted in bold, with its longest edge, i.e., $\tau = \text{Youngest}(\partial(\text{cascade}[\sigma]))$, dotted. When it exists, $\text{cascade}[\text{partner}[\tau]]$ is shown in blue. A persistent pair (τ, σ) is created when $\text{partner}[\tau] = \emptyset$, i.e., when τ coincides with a yellow unpaired edge (rightmost images). In both executions, $\text{Rips}_{\delta(\sigma)}^1$ is shown in light gray.

selves, it can be faster to only store the boundary of each simplex’s cascade $\partial(\text{cascade}(\sigma))$ (instead of the whole cascade itself) and to perform a modulo 2 addition operation on those boundaries when expanding a cascade (line 6 of Alg. 2) [71]. Another acceleration is the preliminary pairing of the *apparent pairs*, pairs of simplices with the same filtration value [71], [72] (some of them appear in Fig. 5 as these dotted red edges whose partner’s cascade is a single triangle).

Algorithm 1: `PairCells`

Input: \mathcal{K}

```

1 for  $\sigma \in \mathcal{K}$  by increasing  $f(\sigma)$  do
2    $\text{partner}[\sigma] \leftarrow \emptyset$ 
3    $\text{cascade}[\sigma] \leftarrow \sigma$ 
4   EliminateBoundaries( $\sigma$ )
5   if  $\partial(\text{cascade}[\sigma]) \neq \emptyset$  then
6      $\tau \leftarrow \text{Youngest}(\partial(\text{cascade}[\sigma]))$ 
7      $\text{partner}[\sigma] \leftarrow \tau$ 
8      $\text{partner}[\tau] \leftarrow \sigma$ 

```

Algorithm 2: `EliminateBoundaries`

Input: $\sigma \in \mathcal{K}$

```

1 while  $\partial(\text{cascade}[\sigma]) \neq \emptyset$  do
2    $\tau \leftarrow \text{Youngest}(\partial(\text{cascade}[\sigma]))$ 
3   if  $\text{partner}[\tau] = \emptyset$  then
4     return
5   else
6      $\text{cascade}[\sigma] \leftarrow$ 
       $\text{cascade}[\sigma] + \text{cascade}[\text{partner}[\tau]]$ 

```

D. Geometric interpretation of persistent homology

Recent boundary matrix reduction-based open-source implementations include *Gudhi* [73], *PHAT* [74] or *Ripser* [72]. In particular, *Ripser* is specialized in the PH computation of

Rips filtrations (given by point clouds or distance matrices) yielding much faster and more memory-efficient execution than previous implementations. However, it is sometimes possible to leverage the Euclidean embedding of point clouds for which we want to compute the PH of the Rips filtration to speed up the computation. In this section, we highlight some known results that link PH^0 and PH^1 of the Rips filtration to some geometric structures defined in Sec. III-A.

The first result is that the set of edges that destroy a PH^0 class of the Rips filtration (i.e., that reduce the number of connected components by 1) is exactly the set of edges of the Euclidean minimum spanning tree (see [7] for example for a proof). It allows to compute the PH^0 of the Rips filtration by constructing the minimum spanning tree of the input point cloud, e.g., with Kruskal’s algorithm based on the union-find data structure [15], in time complexity $\mathcal{O}(n^2\alpha(n^2))$ where α is the inverse of the Ackermann function. This approach is largely used in practice, e.g. in *Ripser* [72].

On the contrary, the edges in the complementary of $\text{MST}(X)$ are the edges that create a PH^1 class [75], possibly with zero persistence – in which case this class dies immediately with a triangle of same diameter. More recently, Koyama et al. [76] showed that the edges of $\text{RNG}(X) \setminus \text{MST}(X)$ are exactly the edges that create a PH^1 class of positive persistence. A corollary is that the quantity $|\text{RNG}(X) \setminus \text{MST}(X)|$ is exactly the number of PH^1 classes with positive persistence (see Fig. 4). Koyama et al. also introduced *Euclidean PH1*, a method that specializes the PH^1 computation for Rips filtrations of point clouds in \mathbb{R}^2 and \mathbb{R}^3 , using the above geometric result. Compared to other Rips PH algorithm like *Ripser*, they improve both running time and memory consumption in this specific case thanks to the construction from the RNG of a reduced Vietoris–Rips complex that features far fewer triangles than the original one, but that has the same PH^0 and PH^1 . This permits to get a much smaller boundary matrix to be reduced.

E. Topological Autoencoders

Our method builds on *Topological Autoencoders* (TopoAE) [1], a dimension reduction technique that combines

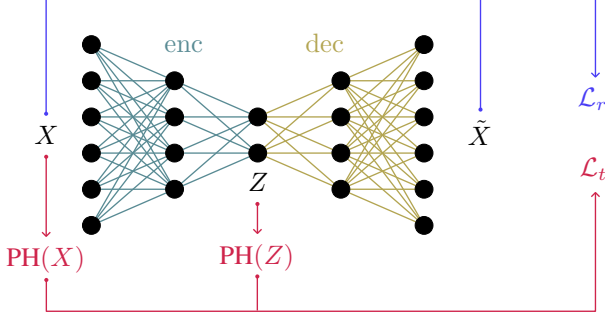


Fig. 6. An autoencoder with reconstruction term \mathcal{L}_r and topological regularization term \mathcal{L}_t . Here both the encoder and the decoder are fully-connected networks with 1 hidden layer.

an autoencoder with a topological feature preservation loss. We therefore briefly summarize this approach below.

Let \mathcal{X} be the input, high-dimensional space and \mathcal{Z} the latent, low-dimensional space. For visualization purposes, in the following we take $\mathcal{Z} = \mathbb{R}^2$. An *autoencoder* [16] is a composition $\text{dec} \circ \text{enc}$ of an *encoder* $\text{enc} : \mathcal{X} \rightarrow \mathcal{Z}$ and a *decoder* $\text{dec} : \mathcal{Z} \rightarrow \mathcal{X}$. We write $Z = \text{enc} X \in \mathcal{Z}$ the representation of an input vector $X \in \mathcal{X}$ and $\tilde{X} = \text{dec}(\text{enc} X)$ its reconstruction. In practice, enc and dec are neural networks, e.g., with one or several fully connected layer(s), possibly with one or several additional convolutional layer(s) if \mathcal{X} represents an image space. The reconstruction loss of an autoencoder is simply the MSE between an input and its reconstruction:

$$\mathcal{L}_r = \|\text{dec}(\text{enc} X) - X\|^2. \quad (4)$$

For constraining autoencoders to preserve topological structures, one can add to this reconstruction term a topological regularization term \mathcal{L}_t which compares some topological abstraction of the input and its low-dimensional representation (Fig. 6). Moore et al. [1] discussed a regularization term considering directly the lengths of carefully selected edges:

$$\mathcal{L}_{\text{TAE}}^d = \|A^X[\pi^d(X)] - A^Z[\pi^d(X)]\|_2^2 + \|A^Z[\pi^d(Z)] - A^X[\pi^d(Z)]\|_2^2, \quad (5)$$

where $A^X[\cdot]$ and $A^Z[\cdot]$ denote evaluating the distance matrix of X and Z respectively, and where $\pi^d(X)$ (resp. $\pi^d(Z)$) denotes all k -critical edges, for any $0 \leq k \leq d$, in X (resp. Z), i.e., the edges that either create or kill a PH^k class of positive persistence (see Sec. III-B).

In practice however, the method is only documented for PH^0 , so that $\pi^0(X) = \text{MST}(X)$ and $\pi^0(Z) = \text{MST}(Z)$ (see Sec. III-D). In that case, the regularization term rewrites as:

$$\mathcal{L}_{\text{TAE}}^0 = \|A^X[\text{MST}(X)] - A^Z[\text{MST}(X)]\|_2^2 + \|A^Z[\text{MST}(Z)] - A^X[\text{MST}(Z)]\|_2^2. \quad (6)$$

The idea of this loss function is to force the length of topologically critical edges in the input to be preserved in the representation (first line of Eq. 6), and reciprocally (second line). More precisely, the second term tries to push away in Z the ends of the edges in $\text{MST}(Z) \setminus \text{MST}(X)$ that are, intuitively, too short in Z . The hope is that at the end of the optimization, the length of both MST's edges match in

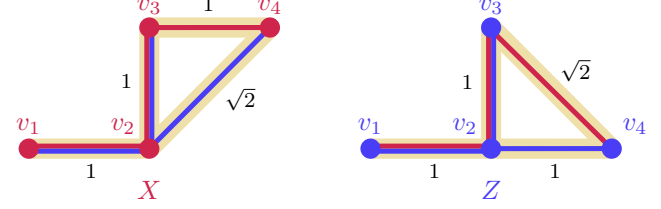


Fig. 7. Notations for the proof of Lem. 1. In this example $\text{MST}(X) = \{\{v_1, v_2\}, \{v_2, v_3\}, \{v_3, v_4\}\}$ (in red) and $\text{MST}(Z) = \{\{v_1, v_2\}, \{v_2, v_3\}, \{v_2, v_4\}\}$ (in blue). Therefore $\mathcal{K} = \{\{v_1, v_2\}, \{v_2, v_3\}, \{v_2, v_4\}, \{v_3, v_4\}\}$ (in yellow). Here $\mathcal{L}_{\text{TAE}}^0(X, Z)$ evaluates as $(\delta_X(\{v_2, v_4\}) - \delta_Z(\{v_2, v_4\}))^2 + (\delta_X(\{v_3, v_4\}) - \delta_Z(\{v_3, v_4\}))^2 = 2(\sqrt{2} - 1)^2$. Note that this provides an example where $\mathcal{L}_{\text{TAE}}^0(X, Z) > 0$ but $\mathcal{D}_{\text{Rips}}^0(X) = \mathcal{D}_{\text{Rips}}^0(Z)$, i.e. the converse of the stated implication (Lem. 1) is not true.

high and low dimension, inducing the same 0-th persistence diagrams (which we show in Sec. IV-A).

Finally, the weights of the autoencoder are optimized iteratively to minimize the value of the loss function. Note that this involves computing the required critical edges of the current representation Z at each iteration.

IV. TOPOLOGICAL AUTOENCODER ANALYSIS

In this section we provide a novel theoretical analysis of the TopoAE loss function [1] and its link with the Wasserstein distance between the persistence diagrams in high and low dimensions. Our aim is to better understand its limitations and the configurations that may cause them.

A. Relation to the Wasserstein distance

We first show below that the topological regularization term $\mathcal{L}_{\text{TAE}}^0$ (Eq. 6) upper bounds the L_2 -Wasserstein distance \mathcal{W}_2 between both 0-dimensional persistence diagrams.

Lemma 1. *For any point clouds X and Z of equal size, we have the following inequality:*

$$\mathcal{W}_2(\mathcal{D}_{\text{Rips}}^0(X), \mathcal{D}_{\text{Rips}}^0(Z))^2 \leq \mathcal{L}_{\text{TAE}}^0(X, Z).$$

Besides, under general position hypothesis (unique pairwise distances), if $\mathcal{L}_{\text{TAE}}^0(X, Z) = 0$, then $\mathcal{D}_{\text{Rips}}^0(X) = \mathcal{D}_{\text{Rips}}^0(Z)$ and the PH^0 pairs are the same, i.e. $\text{MST}(X) = \text{MST}(Z)$.

Proof. Let \mathcal{K} be the (abstract) 1-dimensional simplicial complex $\mathcal{K} = \text{MST}(X) \cup \text{MST}(Z)$ (see Fig. 7). Let $\delta_X : \mathcal{K} \rightarrow \mathbb{R}$ (resp. $\delta_Z : \mathcal{K} \rightarrow \mathbb{R}$) be the simplex diameter function in X (resp. in Z). Because the minimum spanning tree contains exactly all the edges that kill a 0-dimensional persistent homology class, and because $\text{MST}(X) \subset \mathcal{K}$ and $\text{MST}(Z) \subset \mathcal{K}$, we have $\mathcal{D}_{\text{Rips}}^0(X) = \mathcal{D}^0(\delta_X)$ and $\mathcal{D}_{\text{Rips}}^0(Z) = \mathcal{D}^0(\delta_Z)$. Hence,

the following inequalities:

$$\begin{aligned}
& \mathcal{W}_2(\mathcal{D}_{\text{Rips}}^0(X), \mathcal{D}_{\text{Rips}}^0(Z))^2 = \mathcal{W}_2(\mathcal{D}^0(\delta_X), \mathcal{D}^0(\delta_Z))^2 \\
& \leq \sum_{\substack{\sigma \in \mathcal{K} \\ \dim(\sigma) \in \{0,1\}}} |\delta_X(\sigma) - \delta_Z(\sigma)|^2 \quad (\text{by Cellular Wasserstein stability theorem [67]}) \\
& = \sum_{\substack{\sigma \in \mathcal{K} \\ \dim(\sigma)=1}} |\delta_X(\sigma) - \delta_Z(\sigma)|^2 \quad (\text{Rips filtration}) \\
& \leq \sum_{\substack{\sigma \in \text{MST}(X) \\ \dim(\sigma)=1}} |\delta_X(\sigma) - \delta_Z(\sigma)|^2 + \sum_{\substack{\sigma \in \text{MST}(Z) \\ \dim(\sigma)=1}} |\delta_X(\sigma) - \delta_Z(\sigma)|^2 \\
& = \|A^X[\pi^0(X)] - A^Z[\pi^0(X)]\|_2^2 + \|A^Z[\pi^0(Z)] - A^X[\pi^0(Z)]\|_2^2 \\
& = \mathcal{L}_{\text{TAE}}^0(X, Z).
\end{aligned}$$

In particular, when $\mathcal{L}_{\text{TAE}}^0(X, Z) = 0$, then $\mathcal{D}_{\text{Rips}}^0(X) = \mathcal{D}_{\text{Rips}}^0(Z)$. In that case, general position hypothesis (unique pairwise distances) on X and Z – that guarantees the uniqueness of their respective MST – implies $\text{MST}(X) = \text{MST}(Z)$, hence the same PH^0 pairs. \square

This result is, to our knowledge, the first theoretical guarantee that justifies using the original, 0-dimensional version of the TopoAE loss function (Eq. 6) as a regularization term for preserving PH^0 . In particular, if this term is zero, we know that the representation Z has the same PH^0 – and therefore the same 0-th persistence diagram – than the input X .

B. Counter-example for higher dimensional PH

Unfortunately, Lem. 1 does not generalize to higher-dimensional PH. Indeed, as soon as we add the edges that create or destroy PH^1 classes (Sec. III-E), a zero $\mathcal{L}_{\text{TAE}}^1$ loss (Eq. 5) no longer implies equality of the persistence diagrams:

$$\mathcal{L}_{\text{TAE}}^1(X, Z) = 0 \Rightarrow \begin{cases} \mathcal{D}_{\text{Rips}}^0(X) = \mathcal{D}_{\text{Rips}}^0(Z) \\ \mathcal{D}_{\text{Rips}}^1(X) = \mathcal{D}_{\text{Rips}}^1(Z) \end{cases}. \quad (7)$$

Fig. 8 provides a detailed counter-example for two point clouds $X \subset \mathbb{R}^3$ and $Z \subset \mathbb{R}^2$ which illustrates this non-implication. This example shows that preserving the length of topologically critical edges is not enough to guarantee the preservation of PH^k when $k \geq 1$.

V. CASCADE DISTORTION

This section presents a new penalty term called *cascade distortion* (CD) which addresses the above counter-example. This term favors an isometric embedding of the 2-chains filling persistent 1-cycles (i.e., that are computed thanks to the `PairCells` algorithm), leading to a more accurate geometrical representation of the persistent 1-cycles in low dimensions.

A. Formulation

Let \mathcal{P}^k be the set of PH^k pairs with a positive persistence, i.e., $\mathcal{P}^k = \{(\tau, \sigma) \in \mathcal{K}^k \times \mathcal{K}^{k+1} \mid \text{partner}[\tau] = \sigma \text{ and } \delta(\tau) < \delta(\sigma)\}$. We now define the d -dimensional *global cascade*

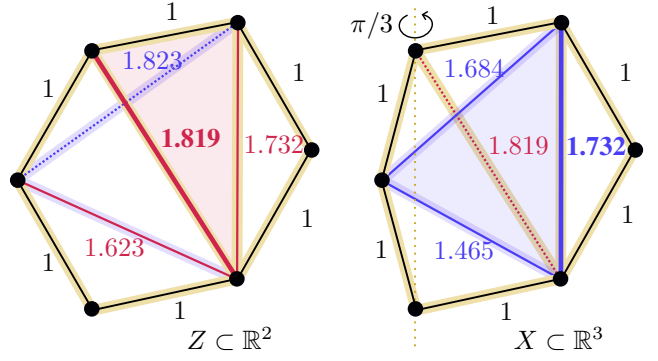


Fig. 8. An example for the non-implication of Eq. 7. The left point cloud Z is in \mathbb{R}^2 and is a deformed regular hexagon; the right one X is in \mathbb{R}^3 and its leftmost point has been rotated with respect to the dotted yellow axis with angle $\pi/3$ (see Sec. B for raw coordinates). Both RNGs are pictured in black and the length of their edges are 1. The triangle that kills the cycle in X (resp. Z) is shown in blue (resp. red) with its longest edge highlighted in bold. For Z , the remaining cascade edge (see Eq. 8) is also shown (its length is 1.623). The 0-th persistence diagrams are the same: $\mathcal{D}_{\text{Rips}}^0(X) = \mathcal{D}_{\text{Rips}}^0(Z) = \{(0, 1) \text{ with multiplicity } 5, (0, +\infty)\}$; but not the 1-th persistence diagrams: $\mathcal{D}_{\text{Rips}}^1(Z) = \{(1, 1.819)\}$ and $\mathcal{D}_{\text{Rips}}^1(X) = \{(1, 1.732)\}$. However, the critical edges considered in $\mathcal{L}_{\text{TAE}}^1$ (i.e., RNG edges and 1-cycle killing edges, highlighted in yellow) have the same length in both X and Z , therefore $\mathcal{L}_{\text{TAE}}^1(X, Z) = 0$. On the contrary, the two additional edges considered in the 1-dimensional *cascade distortion* (highlighted in purple, see Eq. 9) are longer in Z than in X , hence $\mathcal{L}_{\text{CD}}^1(X, Z) > 0$.

skeleton (GCS^d) as the set of edges that appear in the cascade of any PH^k pair with $0 \leq k \leq d$:

$$\text{GCS}^d(X) = \bigcup_{k=0}^d \bigcup_{(\tau, \sigma) \in \mathcal{P}^k} \text{cascade}[\sigma]^{(1)}. \quad (8)$$

In Fig. 5, $\text{GCS}^1(X)$ appears in the bottom-right image as the set of red edges. This leads us to propose the following d -dimensional *Cascade Distortion* (CD) loss function, which looks similar to the original TopoAE loss (Eq. 5), but which constrains the length of all the edges appearing within the global cascade of X , instead of its critical edges only:

$$\mathcal{L}_{\text{CD}}^d(X, Z) = \|A^X[\text{GCS}^d(X)] - A^Z[\text{GCS}^d(X)]\|_2^2 + \|A^Z[\pi^d(Z)] - A^X[\pi^d(Z)]\|_2^2. \quad (9)$$

In practice, we focus our study on $\mathcal{L}_{\text{CD}}^1$ for visualization purposes. Intuitively, the role on the first term (top line of Eq. 9) is to favor an isometric embedding of the input cycles and the 2-chains that fill them, so that their shapes are preserved at best. The second term (bottom line of Eq. 9), like in TopoAE, involves pushing away vertices that are too close in Z , hence penalizing the cycles that exist in Z but not in X . This way, the first term favors a faithful projection of the high-dimensional cycles, while the second term removes spurious low-dimensional cycles from the planar projection. In addition, this loss enables the usage of a dedicated algorithm for the fast computation of $\pi^1(Z)$ at each optimization iteration (Sec. VI).

In practice, $\text{GCS}^1(X)$ is computed using a modified version of `PairCells`, which, similarly to [70], uses a two-step approach. First, the persistence pairs \mathcal{P}^1 with a positive persistence are computed with an efficient, dedicated algorithm,

e.g., *Ripser* [72]. Then, for each pair $(\tau, \sigma) \in \mathcal{P}^1$ in ascending order, we run the `EliminateBoundary` procedure (Alg. 2) from σ until the youngest edge of the boundary $\partial(\text{cascade}[\sigma])$ is τ , storing the cascade edges encountered in the meantime. At each step, $\text{Youngest}(\partial(\text{cascade}[\sigma]))$ forms either an apparent pair (with a triangle that is searched at this moment), or a positive persistence pair that was handled previously. Note that it is mandatory to choose the same order as *Ripser* on the triangles with identical diameter (i.e., the reverse colexicographic order). This is more efficient than a naive execution of `PairCells`, since it benefits from the accelerations of *Ripser*.

B. Relation to TopoAE

The above *Cascade Distortion* term (Eq. 9) can be understood as a generalization of the original TopoAE topological regularization term in that when restricting to PH^0 , both formulations are equivalent.

Lemma 2. *For any point cloud X , $\text{GCS}^0(X) = \text{MST}(X)$. Therefore, the 0-dimensional CD and TopoAE regularization terms are equal: $\mathcal{L}_{\text{TAE}}^0(X, Z) = \mathcal{L}_{\text{CD}}^0(X, Z)$.*

Proof. Let X be a point cloud. First note that for any σ , we have $\sigma \in \text{cascade}[\sigma]$, hence:

$$\text{MST}(X) = \underbrace{\bigcup_{(\tau, \sigma) \in \mathcal{P}^0} \{\sigma\}}_{\text{see Sec. III-D}} \subset \underbrace{\bigcup_{(\tau, \sigma) \in \mathcal{P}^0} \text{cascade}[\sigma]}_{\text{by definition (Eq. 8)}} = \text{GCS}^0(X).$$

Reciprocally, note that for any vertex τ , $\text{partner}[\tau]$ is an edge that kills a PH^0 class, hence is an MST edge. Then, with line 6 (Alg. 2), $\text{cascade}[\sigma]$ writes as the sum of σ and cascades of edges of the form $\text{partner}[\tau]$. Therefore, by recurrence on the edges by increasing length, for any $\sigma \in \text{MST}(X)$, i.e., for any $(\tau, \sigma) \in \mathcal{P}^0$, we have $\text{cascade}[\sigma] \subset \text{MST}(X)$. Hence $\text{GCS}^0(X) \subset \text{MST}(X)$. In the end, $\text{GCS}^0(X) = \text{MST}(X)$. \square

For higher-dimensional PH however, we can only say that $\mathcal{L}_{\text{TAE}}^d(X, Z) \leq \mathcal{L}_{\text{CD}}^d(X, Z)$, i.e., the latter is more restrictive than the former. For instance, for $d = 1$, in the counter-example of Fig. 8 where we had $\mathcal{D}_{\text{Rips}}^1(X) \neq \mathcal{D}_{\text{Rips}}^1(Z)$ but $\mathcal{L}_{\text{TAE}}^1(X, Z) = 0$, the 1-dimensional cascade distortion is here indeed positive : $\mathcal{L}_{\text{CD}}^1(X, Z) > 0$. More generally, $\mathcal{L}_{\text{CD}}^1$ additionally constrains the length of the edges of the 2-chains that fill the persistent 1-cycles, hence favoring an isometric embedding of those chains. Intuitively, this can be understood as trying to preserve the whole *shape* of the 1-cycles, instead of only their birth and death. Although $\mathcal{L}_{\text{CD}}^2$ could be similarly understood as a way to preserve the *shape* of the cavities when projecting to \mathbb{R}^3 , this paper does not further investigate the use of cascade distortion for $d > 1$, as it would be much more computationally expensive.

In the following, we call TopoAE++ the dimensionality reduction technique obtained by replacing in TopoAE the topological regularization term $\mathcal{L}_{\text{TAE}}^0$ with $\mathcal{L}_{\text{CD}}^1$, and by including the acceleration presented in the next section.

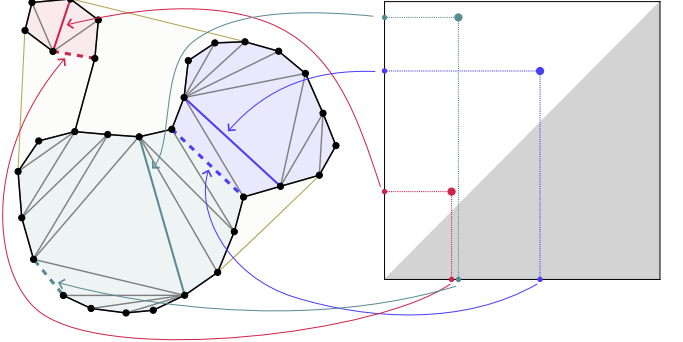


Fig. 9. RNG-polygons (green, blue and red polygons) with their minmax length triangulations (gray edges). The arrows show to which critical edges (birth: dashed; death: continuous) is associated each point of the 1-dimensional persistence diagram. Each birth edge is in the RNG and each death edge is the longest edge of the minmax length triangulations of its RNG-polygon. Missing edges from the convex hull are shown in yellow, as well as the remaining polygons that the convex hull forms with the RNG.

VI. FAST ALGORITHM FOR RIPS PH IN THE PLANE

Because the computation of the persistence diagram of the low-dimensional representation is executed at each step of the optimization process, it is a critical stage in terms of computation time. Therefore, we propose in this section a new fast algorithm that computes PH for the Rips filtration of a two-dimensional point cloud, which is useful when our embedding space is \mathbb{R}^2 , e.g., for visualization purpose. This algorithm is purely geometric and involves no matrix reduction step, contrary to other algorithms (e.g. [72]–[74], [76]), which allows it to be significantly faster and less memory-intensive (see Sec. VII-E1 for timing results).

A. Geometrical results

We rely on the fact that the edges that introduce a cycle are exactly the edges in $\text{RNG}(X) \setminus \text{MST}(X)$ (as previously exploited in the related work [76], see Sec. III-D). Consequently, the number of points in the 1-th persistence diagram is the number of polygons formed by $\text{RNG}(X)$, which is also the cardinal of $\text{RNG}(X) \setminus \text{MST}(X)$. In contrast to previous work [76] (which also exploited boundary matrix reduction), we additionally claim that the critical edges that kill these PH^1 classes can be found efficiently through geometric – rather than algebraic – considerations, namely with a minmax length triangulation of each RNG-polygons (see Fig. 9).

Lemma 3. *In the plane, an edge that intersects an RNG edge kills no PH^1 class of positive persistence.*

Proof outline. Let ab be an edge that intersects an RNG edge pq . Suppose that ab kills a PH^1 class γ of positive persistence. Then ab is the longest edge of two triangles abc and abd , where $acbd$ is a representative 1-cycle of γ , and such that c and d are on both sides of $\text{Lens}(a, b)$. We show that it is always possible to construct a 2-chain whose boundary is $acbd$ and that contains only triangles of diameter $< |ab|$. This 2-chain depends on whether both p and q belong to $\text{Lens}(a, b)$ (Fig. 10, left) or only one of them does (Fig. 10, right). Hence, the class γ is killed before the value $|ab|$, therefore not by ab . See Appendix C for the full proof. \square

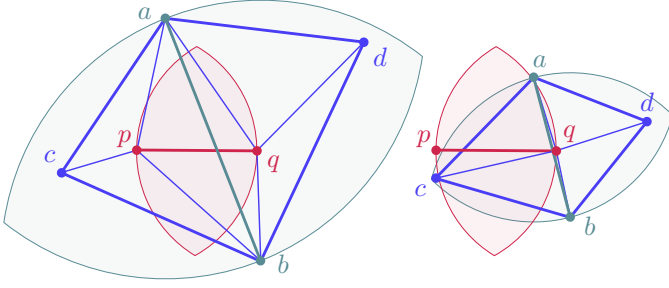


Fig. 10. Notations for proof of Lem. 3. pq (in red) is supposed to be an RNG edge, hence an empty lens. An edge ab (light green) that crosses pq is shown to not be able to kill any PH^1 class of positive persistence.

Therefore, the edges that kill a PH^1 class of positive persistence can only lie inside either an RNG-polygon, or a polygon formed by the RNG and the convex hull of X (Fig. 9). Then, we have the following lemma for each RNG-polygon.

Lemma 4. *Let Π be a RNG-polygon. Under general position hypothesis (unique pairwise distances), the longest edge e_{MML} , of length noted δ_{MML} , of any minmax length triangulation of Π kills a PH^1 class γ with positive persistence for which Π is a representative.*

Proof. Let Π be a RNG-polygon with point set P . Let e_{MML} be the longest edge of the minmax length triangulations of this polygon, which is well-defined with the general position hypothesis. We have the following:

- for diameter threshold $r = \delta_{\text{MML}}$, $\text{Rips}_r(P)$ contains a MML triangulation of Π , which can be seen as a 2-chain whose boundary is Π ;
- for any diameter threshold $r < \delta_{\text{MML}}$, $\text{Rips}_r(P)$ contains no 2-chain whose boundary is Π : otherwise, one could construct a triangulation of Π whose longest edge is of length at most r , hence smaller than δ_{MML} .

Hence, e_{MML} kills a PH^1 class γ with positive persistence for which Π is a representative. \square

Therefore, in the plane, as the number of RNG-polygons is exactly the number of PH^1 classes with a positive persistence, the edges that destroy the latter are exactly the edges found in the above lemma, i.e., that are the longest of the MML triangulations of an RNG-polygon (see Fig. 9).

Finally, for any RNG-polygon, we state a relation between δ_{MML} and the length δ_{Del} of the longest Delaunay edge e_{Del} inside this polygon, enabling the search of e_{MML} among a smaller subset of the polygon's diagonals (see Sec. VI-B).

Lemma 5. *In the plane, the values δ_{MML} and δ_{Del} of an RNG-polygon verify:*

$$\frac{\sqrt{3}}{2} \delta_{\text{Del}} \leq \delta_{\text{MML}} \leq \delta_{\text{Del}}.$$

Proof. Let Π be an RNG-polygon and P its point set. Let $e_{\text{Del}} \in \text{DEL}(P)$ be the longest Delaunay edge inside Π , of length $\delta_{\text{Del}} = |e_{\text{Del}}|$. The right inequality results from the Delaunay triangulation inside Π being a 2-chain whose boundary is Π and whose maximum diameter is δ_{Del} : hence the associated Rips PH^1 class γ is killed at value $\delta_{\text{MML}} \leq \delta_{\text{Del}}$.

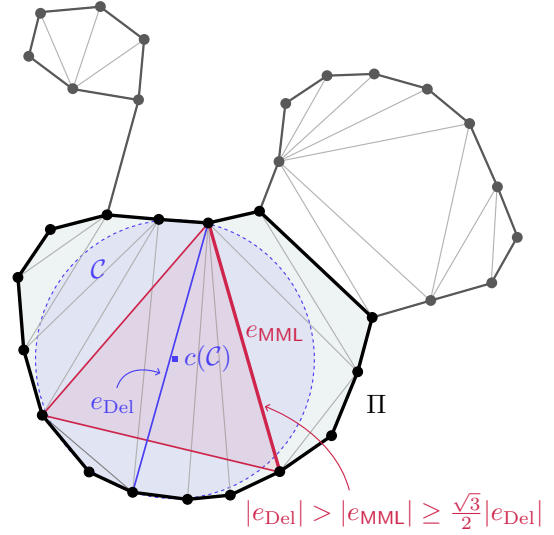


Fig. 11. Notations for the proof of Lem. 5. The RNG-polygon Π (bold black), is such that its Delaunay triangulation (in gray) is not a MML triangulation. Hence, its cycle killing edge e_{MML} (bold red) is shorter than its longest Delaunay edge e_{Del} (blue), i.e., $\delta_{\text{MML}} < \delta_{\text{Del}}$. The circumcircle \mathcal{C} of the longest Delaunay edge e_{Del} contains no points of X in its interior.

For the left inequality, because e_{Del} is a Delaunay edge, there exists a circumcircle \mathcal{C} to e_{Del} of radius $r(\mathcal{C}) \geq |e_{\text{Del}}|/2$ that contains no other point of P (see Fig. 11). Now any 2-chain with Π as boundary has to contain the center $c(\mathcal{C})$ of that circle. However, the smallest triangles with no vertex within \mathcal{C} and that contain $c(\mathcal{C})$ are exactly the equilateral triangles circumscribed by \mathcal{C} , and their side length is $\sqrt{3}r(\mathcal{C}) \geq \frac{\sqrt{3}}{2}|e_{\text{Del}}|$. Therefore, the associated Rips PH^1 class γ is killed by a triangle τ of diameter at least $\frac{\sqrt{3}}{2}|e_{\text{Del}}|$, hence $\frac{\sqrt{3}}{2}\delta_{\text{Del}} \leq \delta_{\text{MML}}$. \square

B. Algorithm description

Leveraging the above results, we introduce a fast algorithm that computes PH for the Rips filtration of a 2-dimensional point cloud. It is summarized in Alg. 3 and we describe below more precisely the different stages.

Algorithm 3: 2D Rips persistence method overview

Input: Point cloud $X \subset \mathbb{R}^2$
Output: Persistence diagrams $\mathcal{D}_{\text{Rips}}^0(X)$ and $\mathcal{D}_{\text{Rips}}^1(X)$ with associated simplices

- 1 Compute the Delaunay triangulation $\text{DEL}(X)$
- 2 Compute the Urquhart graph $\text{UG}(X)$
- 3 Apply Kruskal's algorithm on $\text{UG}(X)$ to compute $\text{MST}(X)$ and obtain $\mathcal{D}_{\text{Rips}}^0(X)$
- 4 Check the emptiness of the lens of the edges in $\text{UG}(X) \setminus \text{MST}(X)$ to compute $\text{RNG}(X)$
- 5 For each RNG-polygon, find its local minmax length triangulation's longest edge (Alg. 4)
- 6 Apply Kruskal's algorithm on the dual $\text{RNG}(X)$ graph to obtain $\mathcal{D}_{\text{Rips}}^1(X)$

Algorithm 4: Find the longest edge of a minmax length triangulation of an RNG-polygon of X

Input: Points $P \subset X$ of an RNG-polygon
Input: Length δ_{Del} of the longest Delaunay edge
Output: Edge that destroy the associated 1-cycle

```

1 candidates  $\leftarrow \{\}$ 
2 for  $e = v_1v_2 \in \binom{P}{2}$  s.t.  $|e| \in \left[ \frac{\sqrt{3}}{2} \delta_{\text{Del}}, \delta_{\text{Del}} \right]$  do
    // check if  $e$  is a 2-edge
    if LeftLens( $e$ )  $\neq \emptyset$  and RightLens( $e$ )  $\neq \emptyset$  then
        // check if  $e$  is expandable
        for  $x \in \text{LeftLens}(e)$  do
            if RightLens( $v_1x$ )  $= \emptyset$  and
                RightLens( $xv_2$ )  $= \emptyset$  then
                    LeftExpandable  $\leftarrow$  true
                    break
        for  $y \in \text{RightLens}(e)$  do
            if RightLens( $v_2y$ )  $= \emptyset$  and
                RightLens( $yx_1$ )  $= \emptyset$  then
                    RightExpandable  $\leftarrow$  true
                    break
        if LeftExpandable and RightExpandable then
            candidates  $\leftarrow$  candidates  $\cup \{e\}$ 
    end if
end for
14 return min(candidates, |·|)
```

a) *Delaunay triangulation:* We use CGAL [77] to compute the Delaunay triangulation, with identifiers on vertices and triangles. This implementation deals with the boundary (simplices on the convex hull) with a virtual point at infinity.

b) *Relative neighborhood graph:* To compute $\text{RNG}(X)$, we first compute $\text{UG}(X)$ by keeping Delaunay edges whose link (made of two points) is outside their lens. We then apply Kruskal’s algorithm (which uses a union-find data structure [15]) on $\text{UG}(X)$ to compute $\text{MST}(X)$, of which $\mathcal{D}_{\text{Rips}}^0(X)$ can be deduced (see Sec. III-A and Sec. III-D). Then, checking the emptiness of the lens of the edges in $\text{UG}(X) \setminus \text{MST}(X)$ using disk queries on a precomputed k-d tree, we determine whether they belong to $\text{RNG}(X)$, and construct a data structure that represents $\text{RNG}(X)$ and its polygons (see next paragraph).

c) *Data structure for RNG-polygons:* During the computation of $\text{UG}(X)$ and $\text{RNG}(X)$, we maintain a union-find data structure on Delaunay triangles that permits to deduce efficiently the RNG-polygons. More precisely, as soon as we encounter a non-RNG edge (either during $\text{UG}(X)$ computation or during $\text{RNG}(X)$ refinement), we merge (if not already merged) the two classes associated with its two adjacent triangles. We also keep for each current class the longest deleted Delaunay edge, which needs to be maintained at each merge. Besides, we store $\text{UG}(X)$ and $\text{RNG}(X)$ edges as quad-edges (i.e., an edge is stored as the identifiers of its two extremities and the identifiers of its two adjacent triangles). This allows an implicit representation of the RNG-polygons, each of which is associated with a root of the union-find data

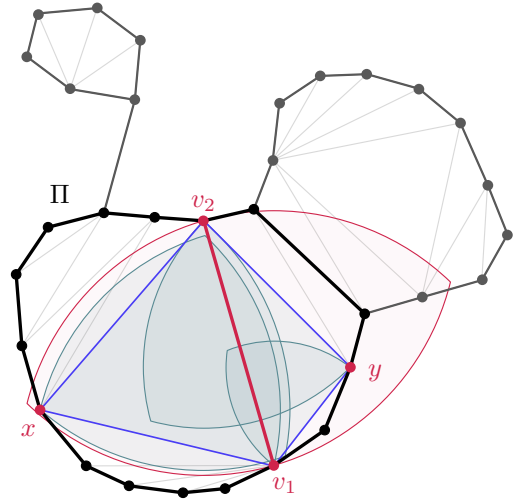


Fig. 12. Illustration of the expandability – tested by Alg. 4 – of the 2-edge $e = v_1v_2$. Indeed there exists $x, y \in \text{Lens}(e)$ (red area) on either side of e such that the “inner” half-lenses (green areas) of the edges v_1x , xv_2 , v_2y , yx_1 are empty. Thus, there exists a planar triangulation of Π whose longest edge is e . Besides, e happens to be the smallest of the expandable 2-edges in Π : e is therefore the longest edge of the MML triangulations of Π .

structure over triangles. For the next stage, we also recover the vertices associated with each polygon.

d) *Minmax length triangulations:* Now all we need is to find the edges that kill persistent cycles: using Lem. 4, we search the longest edge e_{MML} of a MML triangulation of each polygon. For that we partially follow the algorithm described in [61] that computes MML triangulations in quadratic time, even though there is no need here to compute a full triangulation since we only need its longest edge. Therefore for each RNG-polygon, we enumerate the polygon diagonals with length between $\frac{\sqrt{3}}{2} \simeq 0.866$ and 1 times the length of the longest deleted Delaunay edge within the polygon (see Lem. 5). Among them, we search the smallest that is an *expandable 2-edge* (a property introduced in [61] that allows an edge to be the longest of a triangulation of the polygon, see Sec. A-B for more details) using disk queries on a k-d tree on the vertices of the polygon (see Fig. 12 and Alg. 4).

e) *Persistent pairs:* The last step consists in pairing edges that create cycles with those that kill them (a cycle-creating edge is not necessarily associated with a killer edge of an adjacent polygon, in case of nested cycles). We solve this relying on duality, an overall strategy also employed in the seminal persistence algorithm [65]. Specifically, for our setup, we compute PH^0 of the dual of $\text{RNG}(X)$ with opposite filtration values, which is the PH^1 of the input. In other words, we apply Kruskal’s algorithm on a dual graph where dual nodes are RNG-polygons Π with filtration value $-\delta_{\text{MML}}(\Pi)$, and where dual edges are cycle-creating edges $e \in \text{RNG}(X) \setminus \text{MST}(X)$ with filtration value $-|e|$.

C. Parallelization

Several stages can be parallelized for accelerating the running time. The most critical stage is the computation of minmax length triangulations (it represents around 50% of the computation time on average in sequential for uniform

point clouds). It can be naively parallelized on the different RNG-polygons. However, these polygons can be of varying sizes, leading to a poor speed-up in some cases. Instead, we develop a slightly more efficient parallelization, which consists in storing in a single array every candidate edge (of length in $\left[\frac{\sqrt{3}}{2}\delta_{\text{Del}}, \delta_{\text{Del}}\right]$) of every polygon, and to parallelize the expandability checks on this array.

Finally, other stages can be easily parallelized with a less noticeable effect, such as using a parallel sorting implementation for sorting the $\text{UG}(X)$ edges by length (before applying Kruskal's algorithm on them to get $\text{MST}(X)$).

D. Obstacles to generalization

Generalizing this approach to higher-dimensional ambient space (e.g., \mathbb{R}^3) and/or higher-dimensional homology (e.g., PH^2) is difficult. Indeed, the fact that edges introducing a cycle are Delaunay edges does not hold for higher-dimensional homology: a triangle that introduces a cavity (i.e., a PH^2 class) is not necessarily a Delaunay triangle. Furthermore, we rely heavily on duality to efficiently compute "codimension 1" persistent homology (i.e., PH^1 in \mathbb{R}^2), which cannot be used as is to compute PH^1 in \mathbb{R}^3 , for example.

VII. RESULTS

This section presents both qualitative and quantitative experimental results. All results were obtained on a laptop computer with 64 GB of RAM, a Core i7-13850HX CPU (8 cores at 5.3 GHz and 12 cores at 3.8 GHz), and a RTX 2000 GPU. We implemented our method in C++ (with the libraries OpenMP, LibTorch [78] and CGAL [77]) as modules for TTK [79], [80]. We used as encoder (resp. decoder) a fully connected network with two hidden layers of size 128 and 32 (resp. 32 and 128), with ReLU activation functions, and batch normalization. For each experiment, we performed 1000 iterations of the Adam optimizer [81] with a learning rate fixed at 0.01. See Appendix E for a more detailed study of hyperparameter selection.

A. Test data

We present results on synthetic, three-dimensional datasets in Fig. 1, which have been specifically designed to include clearly salient topological features. The first one consists in 3 Gaussian clusters, and features 3 significantly persistent PH^0 pairs. The second one consists in points sampled around an ellipse twisted along its major axis, and features one significantly persistent PH^1 pair. The third one consists in points sampled around the edges of a tetrahedron (i.e., the complete K_4 graph which is planar) and features 3 significantly persistent PH^1 pairs. We also consider a stress case in Fig. 13, with a dense point cloud sampling the complete K_5 graph embedded in \mathbb{R}^3 (i.e., 5 vertices in 3D, all pairwise connected by an edge). Since K_5 is a non-planar graph, the resulting 3D persistent generators (which follow the edges of K_5) cannot be projected to the plane without intersections. Then, it is not possible to project this stress case to the plane faithfully with respect to PH^1 , as the intersections of the projected 3D generators create additional, short cycles in 2D.

Dataset	Nature	Dimension (h)	Size (n)	Fig.
3Clusters	Synthetic	3	800	
Twist	Synthetic	3	100	Fig. 1
K_4	Synthetic	3	300	
K_5	Synthetic	3	500	Fig. 13
COIL-20-1	Acquired	4096	72	
MoCap	Acquired	62	138	Fig. 14
SingleCell	Simulated	1170	243	

TABLE I
SUMMARY OF DATASETS.

We present results on real-life, acquired or simulated, high-dimensional, cycle-featuring datasets in Fig. 14. COIL-20 [82] is an image dataset with 20 classes, each one containing 72 grayscale 64×64 images. Each class consists in a single object (e.g., a rubber duck) viewed from 72 evenly spaced angles, so that the images within each class live on a manifold that is homeomorphic to a circle. This leads to significantly persistent pairs when computing the PH^1 of the input endowed with the Euclidean metric between the images. Cyclic features may also appear in motion capture data [83]. Hence, we also evaluate our approach on a dataset extracted from the CMU motion capture database [84], which records a human subject doing some periodic movement (e.g., walking or running), each frame consisting in 62 skeleton joint angles measurements. Finally, data from biological processes can also feature meaningful cycles like in single-cell omics [85], a field that aims at sequencing single cells. This enables the observation of gene expression within individual cells at different stage of the cell cycle (resting, growth, DNA replication, mitosis). Specifically, we used the simulated dataset "cyclic_2" [86], which features a significantly persistent PH^1 pair. See Tab. I for a summary of the presented datasets.

B. Quantitative criteria

In order to evaluate the topological accuracy of the representations generated by our approach, we compute the L_2 -Wasserstein distance (see Sec. III-B) between the 1-dimensional persistence diagrams of the input X and the low-dimensional representation Z :

$$\text{PDW}^1(X, Z) = \mathcal{W}_2(\mathcal{D}_{\text{Rips}}^1(X), \mathcal{D}_{\text{Rips}}^1(Z)).$$

This quantity, which we want to be as low as possible, summarizes in some measure the extent to which similar cycles exist in the two point clouds. However, as persistence diagrams lose information – they are in particular invariant to permutations in the point clouds – it does not convey whether the set of vertices involved in these cycles are the same, in contrast to TopoAE-like loss functions.

We also compute the metric distortion \mathfrak{D} , which should also be as low as possible, expressed as the root mean squared error (RMSE) between the pairwise distances in X and those in Z – which is what MDS-like methods typically minimize:

$$\mathfrak{D}(X, Z) = \sqrt{\frac{1}{n} \sum_{i < j} (\|X_i - X_j\|_2 - \|Z_i - Z_j\|_2)^2}.$$

We refer the reader to Appendix D-A for a description of other quality scores often considered in the DR literature (see Appendix D-B for experiments with these indicators).

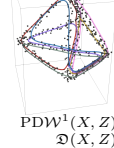
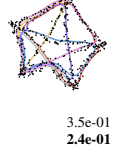
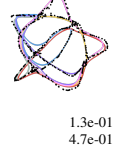
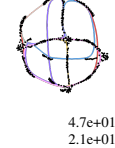
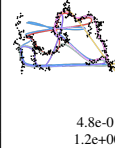
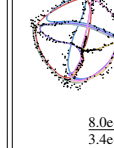
Input	Global methods		Locally topology-aware methods			Globally topology-aware methods			TopoAE++	
	PCA [2]	MDS [3]	Isomap [4]	t-SNE [5]	UMAP [6]	TopoMap [7]	TopoAE [1]	TopoAE+ \mathcal{W}^1 [8]		
K_5 ($n = 500$)										
$PDW^1(X, Z)$	2.8e-01 3.1e-01 0.00043	3.5e-01 2.4e-01 0.59	1.3e-01 4.7e-01 0.088	4.7e+01 2.1e+01 0.63	9.7e-01 9.8e+00 0.14	4.8e-01 1.2e+00 0.063	1.6e-01 9.2e-01 29	2.2e-03 8.6e-01 170	8.0e-02 3.4e-01 6.0	

Fig. 13. Comparison of DR methods on a stress case, i.e., a point cloud sampled around the edges of the complete K_5 graph embedded in 3D. It features 6 significantly persistent PH^1 pairs, and a generator for each is represented with a curve of distinct color. As K_5 is a non-planar graph, this point cloud cannot be projected faithfully in 2D in a topological sense (i.e., the high-dimensional persistent generators cannot be projected to the plane without intersections). Despite this, our method (TopoAE++) achieves a competitive Wasserstein distance.

C. Competing approaches

We compare our approach to global methods (PCA [2], MDS [3]) that do not take topology into account. We also compare to several locally topology-aware methods (Isomap [4], t-SNE [5], UMAP [6]) that are able to consider the local manifold structure of the data but that might fail to project faithfully the overall structure. Regarding previously documented globally topology-aware methods, although TopoMap [7] preserves exactly PH^0 and TopoAE [1] preserves PH^0 in the sense of Lem. 1, both methods have no guarantee about PH^1 . In addition, we show the results of the method suggested in [8], which we denote TopoAE+ \mathcal{W}^1 and which consists in adding $PDW^1(X, Z)$ to the TopoAE loss $\mathcal{L}_{\text{TAE}}^0$. Both terms in the loss are given the same weights. It is then supposed to give the best results in terms of $PDW^1(X, Z)$ values and therefore make the cycles in X and Z as similar (i.e., in number, in size) as possible. However, as explained in Sec. VII-B, $PDW^1(X, Z)$ is not sensible to which simplices are involved in the cycles, and the cycles in Z might be created between simplices that do not belong to a cycle in X .

For PCA, MDS, Isomap and t-SNE, we used the implementations in scikit-learn [87] (with default parameters except Isomap for which the number of neighbors is set to 8); for UMAP, the Python package umap-learn provided by the authors; and for TopoMap, the existing implementation in TTK. For TopoAE-like approaches, we used our own implementation, with Ripser [72] as latent space PH^1 algorithm for TopoAE and TopoAE+ \mathcal{W}^1 , and Alg. 3 for TopoAE++. For non-deterministic methods (i.e., TopoAE, TopoAE+ \mathcal{W}^1 and TopoAE++ which rely on a stochastic optimization of a neural network with a random initialization), we performed 10 runs and kept the result with the best $PDW^1(X, Z)$ (see Appendix F for more information on this stochastic behavior).

D. Result analysis

1) *Qualitative analysis:* Our visual validation approach involves computing a generator for each significantly persistent pair in the input and observing their low-dimensional projections. These generators should ideally be projected without self-intersection and coincide with the cycles in the low-dimensional representation. In such a case, the output would be considered to faithfully represent the high-dimensional cycles.

In the depicted examples, TopoAE++ succeeds in projecting the cycles from the input in this visual sense, whenever possible (with the exception of K_5 , for which a faithful

planar projection is not possible, see Sec. VII-A). It also tends to preserve the *shape* of the cycles. For example, *Twist* (Fig. 1) is projected with the original ellipse shape preserved, but without torsion. Similarly, in *COIL-20-1* (Fig. 14), the high-dimensional cycle has a stretched shape (since the rubber duck has a similar silhouette when viewed from the front and back, but not when viewed from the left and right), which TopoAE++ takes into account (views from the left and right corresponds to the "ends" of the stretched planar cycle). *MoCap* (Fig. 14) comes from the capture of a subject performing a translation in addition to its periodic movement (running). It is therefore projected to a spiral shape, where the longest edge of the projection of the input cycle (appearing in lavender) corresponds to the same body configuration during the running cycle, but at two different locations. Finally, *SingleCell* (Fig. 14) is difficult to project in the plane as it presents points that lie on a cycle but are distant from each other due to the high dimensionality: TopoAE++ takes that into account and its result can be interpreted as a compromise between preserving PH^0 and PH^1 .

On contrary, global methods (PCA, MDS) do not guarantee the preservation of these cycles (see, e.g., their results on *Twist*, Fig. 1, and *COIL-20-1*, Fig. 14), while locally topology-aware methods sometimes fail to project them correctly (e.g., t-SNE and UMAP break apart the cycles in K_4 , Fig. 1, and *SingleCell*, Fig. 14, when projecting). In addition, even if the cycle is visually correctly projected, these methods tend to forget the *shape* of the cycle (e.g., Isomap projects *Twist*, Fig. 1, and *COIL-20-1*, Fig. 14, as almost perfect circles). Finally, as expected, previously documented globally topology-aware methods generally fail to faithfully project the cycles, as they only incorporate constraints on PH^0 (TopoMap, TopoAE) or on the Wasserstein distance PDW^1 (TopoAE+ \mathcal{W}^1), but not on PH^1 (see the next paragraph).

2) *Quantitative analysis:* From a more quantitative point of view, in the examples shown, TopoAE++ generally produces the second best PDW^1 after TopoAE+ \mathcal{W}^1 , both significantly better than all other methods for this metric. However, as TopoAE+ \mathcal{W}^1 directly optimizes PDW^1 and forgets the simplices involved in PH^1 pairs, the vertices involved in planar cycles (i.e., corresponding to the points of $\mathcal{D}_{\text{Rips}}^1(Z)$) do not match those involved in input cycles (i.e., corresponding to the points of $\mathcal{D}_{\text{Rips}}^1(X)$). This leads to a good PDW^1 metric but a poor projection. For instance, in *Twist* (Fig. 1), TopoAE+ \mathcal{W}^1 creates a cycle (the top one) that has the right birth and

Input	Global methods		Locally topology-aware methods			Globally topology-aware methods			TopoAE++	
	PCA [2]	MDS [3]	Isomap [4]	t-SNE [5]	UMAP [6]	TopoMap [7]	TopoAE [1]	TopoAE+ \mathcal{W}^1 [8]		
COIL-20-1 ($n = 72$)										
	$\text{PDW}^1(X, Z)$ $\mathcal{D}(X, Z)$ t (s)	1.2e+01 2.9e+00 0.0071	1.0e+01 2.0e+00 0.086	6.0e+02 2.1e+01 0.083	1.3e+01 4.9e+00 0.30	1.2e+01 6.2e+00 2.5	2.7e+01 7.2e+00 0.14	7.5e+00 8.2e+00 2.0	9.1e-02 6.7e+00 4.0	$1.6e-02$ 1.9e+01 2.4
MoCap ($n = 138$)										
	$\text{PDW}^1(X, Z)$ $\mathcal{D}(X, Z)$ t (s)	2.1e+03 2.4e+01 0.041	1.9e+03 1.7e+01 0.25	1.0e+04 1.3e+02 0.11	1.6e+03 9.9e+01 0.33	1.5e+03 1.0e+02 2.6	2.1e+03 8.5e+01 0.056	1.2e+03 2.6e+01 3.1	9.4e+00 5.6e+01 12	$1.2e+01$ 2.9e+01 3.4
Single-ele11 ($n = 243$)										
	$\text{PDW}^1(X, Z)$ $\mathcal{D}(X, Z)$ t (s)	3.0e+03 3.1e+01 0.0089	3.1e+03 2.3e+01 0.77	1.8e+05 4.8e+02 0.019	1.8e+03 9.6e+01 0.33	1.8e+03 1.0e+02 2.5	2.8e+04 1.2e+03 0.023	1.8e+03 9.8e+01 7.6	6.4e+02 3.2e+02 27	$8.6e+02$ 1.5e+02 6.0

Fig. 14. Comparison of DR methods on three real-life, acquired or simulated, high-dimensional datasets (see Sec. VII-A for a description) that all feature a single significantly persistent PH^1 pair. A generator for this pair is projected down to 2D, in transparency and slightly smoothed (with a color map depicting its arc-length parameterization). Quantitatively, our approach (TopoAE++) achieves a competitive Wasserstein distance. Qualitatively, it generates fewer crossings of the projected high-dimensional persistent generator.

death – while the bottom loop has a persistence close to zero – to cancel out PDW^1 ; yet the original cycle is poorly projected, with a self-intersection. Similarly, on K_5 (Fig. 13), TopoAE+ \mathcal{W}^1 places the points in order to have 6 persistent cycles with the right birth and death to cancel out PDW^1 , while TopoAE++ tries to preserve PH^1 , which is impossible here due to the non-planarity of K_5 .

The distortion metric is higher with TopoAE++, than in global methods (PCA, MDS) which directly minimize it (by design for MDS). It can be seen as a necessary compromise to faithfully project cycles (e.g., Twist, Fig. 1, requires distortion to be untwisted in 2D; the cycle in COIL-20-1, Fig. 14, which is folded up in high dimension, requires distortion to be unfolded). See Fig. 19 of Appendix D for additional common DR indicators (measuring the preservation of both global and local distances), along with a companion discussion.

Fig. 15 provides further evaluations of the internal aspects of our approach. Specifically, for the counter-example of Fig. 8, it compares projections obtained by minimizing a naive extension of [1] to PH^1 ($\mathcal{L}_{\text{TAE}}^1$, Eq. 5) and our novel loss ($\mathcal{L}_{\text{CD}}^1$, Eq. 9). In this example, while the optimization achieves a virtually zero value for both losses, a clear gap occurs between the persistence diagrams $\mathcal{D}_{\text{Rips}}^1(Z_{\text{TAE}})$ and $\mathcal{D}_{\text{Rips}}^1(X)$, while $\mathcal{D}_{\text{Rips}}^1(Z_{\text{CD}})$ coincides with $\mathcal{D}_{\text{Rips}}^1(X)$. This indicates that $\mathcal{L}_{\text{CD}}^1$ enables a better preservation of the persistent homology of the input Z . This gain in topological accuracy is further evaluated in Fig. 16, which compares the resulting Wasserstein distances ($\text{PDW}^1(X, Z)$) for our real-life datasets. In particular, we observe in this figure that, while both losses do not produce intersections in the projection of the high-dimensional generator (colored curve), projections based on our novel loss improve topological accuracy by 48% on average. This illustrates that our novel loss produces projections which are more faithful to the input data, in terms

of the number, size and shape of its cyclic patterns.

E. Time performance

1) *Fast 2D persistence computation*: We compared our persistence algorithm (Alg. 3) for point clouds in \mathbb{R}^2 to the following more generic Rips PH^0 and PH^1 implementations: *Gudhi* [73] (a generic implementation that handles various filtrations), *Ripser* [72] (a specialization to Rips filtrations that can be applied to any point cloud in \mathbb{R}^d or distance matrix), and *Euclidean PH1* [76] (that works theoretically for any point cloud in \mathbb{R}^d , but implemented only for $d = 2$ or $d = 3$). We observe that on uniformly sampled point clouds, the running time asymptotic behavior is roughly cubic (with regard to the number of input points) for *Gudhi* and quadratic for *Ripser*, while it remains close to being linear for *Euclidean PH1* and our algorithm. However, our approach offers a speedup of about 2 orders of magnitudes compared to *Euclidean PH1* (see Fig. 17). The speedup seems even more noticeable with points clouds sampled next to a circle which creates one high-persistence pair in the 1-dimensional persistence diagram and particularly slows down *Euclidean PH1* (see Fig. 18). Finally, we have observed empirically that the use of Lem. 5 in Alg. 4 (i.e., checking expandability only for the edges of length in $\left[\frac{\sqrt{3}}{2}\delta_{\text{Del}}, \delta_{\text{Del}}\right]$) enables discarding 84% of the possible polygon diagonals on average, which significantly contributes to the reported speedup.

2) *Overall DR approach*: TopoAE++ can hardly compete with conventional DR methods (PCA, MDS, Isomap, t-SNE) in terms of computation time. However, this must be put into perspective. First, we construct a complete projection from the input space \mathcal{X} to the latent space \mathbb{R}^2 , and not just a projection of the point cloud X (i.e., we can project a new point, at the low price of one evaluation of the encoder network). Second, we incorporate constraints from persistent homology, which is computationally expensive by nature.

However, our fast 2D Rips PH algorithm (Sec. VI) manages to overcome the runtime overhead due to the computation of PH^1 of Z at each iteration of the optimization. Indeed, comparing TopoAE++ with TopoAE+ \mathcal{W}^1 – which also requires this computation, implemented with *Ripser* – we observe a speedup by a factor of 2 to 20 in the presented examples. The experiments from Fig. 16 (comparing TopoAE++ to a naive extension of [1] to PH^1) report compatible speedups (3.7 on average). In addition, TopoAE++ is sometimes even faster than TopoAE although the latter only computes PH^0 , both initially for the input X and at each optimization step for Z .

F. Limitations

The first obvious limitation is of a fundamental nature: there are point clouds for which there is no planar embedding that is faithful with regard to the PH^1 (see Fig. 13 and its description, Sec. VII-A). Besides, like many other topological methods, we are limited in the size of the input due to the initial PH computation, if only in terms of memory. Specifically, *Ripser*, which is commonly considered as the gold standard implementation for Rips filtrations in high dimensions, runs out of memory on a 64 GB machine when computing the PH^1 of around 50,000 points. This limitation could be addressed by batch processing or subsampling approaches (see, e.g., [1]). In addition, as with the original TopoAE, unsatisfactory results may occur when the minimization of the topological regularization term is not successful (i.e., stuck in a "bad" local minimum). In our experiments, as for TopoAE and TopoAE+ \mathcal{W}^1 , this was mitigated by running 10 times the projection with a random initialization, and considering as an output the projection minimizing $\text{PDW}^1(X, Z)$. More sophisticated strategies could be considered in the future, such as using a locally topology-aware method (e.g., UMAP) for initialization, or penalizing the self-crossings of the input persistent generators during optimization to help escape bad local minima. Finally, the proof of Lem. 1 does not work with higher-dimensional homology, as taking $\text{GCS}^1(X) \cup \text{GCS}^1(Z)$ does not allow to recover $\mathcal{D}_{\text{Rips}}^1(X)$ and $\mathcal{D}_{\text{Rips}}^1(Z)$ like in 0-dimensional homology. Therefore, we have no theoretical guarantee that our cascade distortion loss function upper bounds the Wasserstein distance

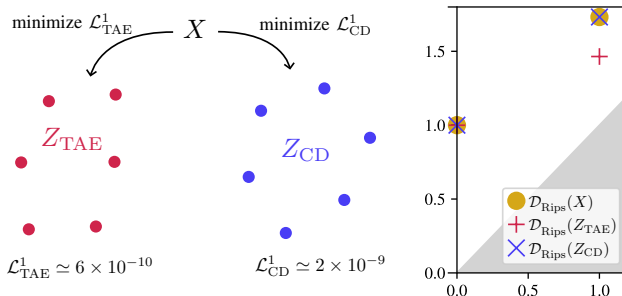


Fig. 15. Topological accuracy comparison between projections obtained with the loss $\mathcal{L}_{\text{TAE}}^1$ (a naive extension of [1] to PH^1 , Eq. 5) and our cascade distortion ($\mathcal{L}_{\text{CD}}^1$, Eq. 9) on the counter-example $X \in \mathbb{R}^3$ of Fig. 8, producing the 2D embeddings Z_{TAE} and Z_{CD} respectively (left). In this example, the optimization achieved a virtually zero value for both losses. However, in the space of persistence diagrams, $\mathcal{D}_{\text{Rips}}^1(Z_{\text{TAE}})$ does not match $\mathcal{D}_{\text{Rips}}^1(X)$, while $\mathcal{D}_{\text{Rips}}^1(Z_{\text{CD}})$ coincides with it (right).

between the persistence diagrams, despite its experimental ability to accurately preserve the cycles. However, we have not found a counter-example yet, similar to the example presented in Fig. 8. If such a bound exists, finding it would require tools beyond those used in this paper. Therefore, answering this question is left to future work.

VIII. CONCLUSION

We have introduced TopoAE++, a dimensionality reduction method aiming at accurately visualizing the cyclic patterns present in high dimensional data. For this, we revisited TopoAE [1], provided a novel theoretical analysis of its original formulation for PH^0 , and introduced a new generalization to PH^1 . We have shown experimentally that our novel projection provides an improved balance between the topological accuracy and the visual preservation of the input 1-cycles. As a side benefit of our work, to overcome the computational overhead due to the PH^1 computation, we have presented a novel, fast, geometric algorithm that computes Rips PH for planar point clouds, which may be of independent interest.

In future work, cleverer initializations and the possibility to handle automatically bad local minima during the minimization, e.g., by penalizing self-intersections of input generators, could be investigated. Besides, an interesting extension would be to generalize the method to either higher-dimensional latent spaces (e.g., $\mathcal{Z} = \mathbb{R}^3$, still for visualization purposes), or to constraints on higher-dimensional homology (e.g., constraining PH^2 to preserve the *cavities*, by optimizing $\mathcal{L}_{\text{CD}}^2$ instead of $\mathcal{L}_{\text{CD}}^1$). However, this might prove computationally challenging, since it would require computing PH^2 in low dimension at each iteration while our fast planar Rips PH^1 algorithm does not seem easily generalizable to such a context. Finally, another interesting extension would be to consider other filtrations of specific interest for the applications.

ACKNOWLEDGMENTS

This work is partially supported by the European Commission grant ERC-2019-COG "TORI" (ref. 863464, <https://erc-tori.github.io/>); and by ANR-23-PEIA-0004 (PDE-AI <https://pde-ai.math.cnrs.fr/>).

	COIL-20-1	MoCap	SingleCell
$\mathcal{L}_t = \mathcal{L}_{\text{TAE}}^1$			
PDW ¹ (X, Z)	3.2e-02	3.0e+01	1.3e+03
t (s)	5.9 (2.4)	15 (3.3)	26 (5.9)
$\mathcal{L}_t = \mathcal{L}_{\text{CD}}^1$			
PDW ¹ (X, Z)	1.6e-02	1.2e+01	8.6e+02
t (s)	2.4	3.4	6.0

Fig. 16. Topological accuracy comparison ($\text{PDW}^1(X, Z)$) between projections obtained with the loss $\mathcal{L}_{\text{TAE}}^1$ and our cascade distortion $\mathcal{L}_{\text{CD}}^1$, for our real-life datasets. For $\mathcal{L}_{\text{TAE}}^1$, we report the runtime with the gold standard for Rips persistence computation [72] as well as, in parentheses, with our novel planar Rips persistence computation algorithm (Sec. VI). On average, projections using our novel loss ($\mathcal{L}_{\text{CD}}^1$), combined with our fast planar Rips persistence algorithm, improve topological accuracy by 48%, with a runtime improvement of 71%.

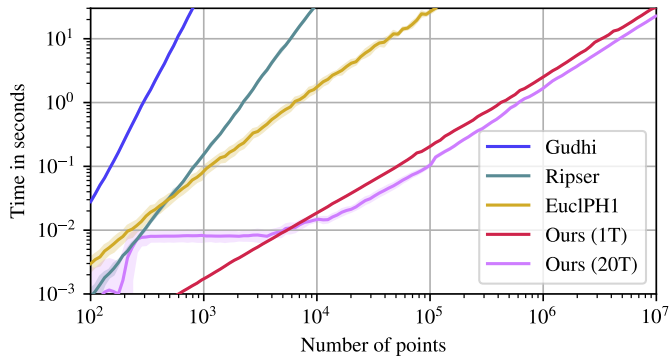


Fig. 17. Comparison of Rips persistence computation times between *Gudhi*, *Ripser*, *Euclidean PHI* and our algorithm (on a single thread, 1T, and on 20 threads, 20T), on point clouds randomly, uniformly distributed over $[0, 1]^2$.

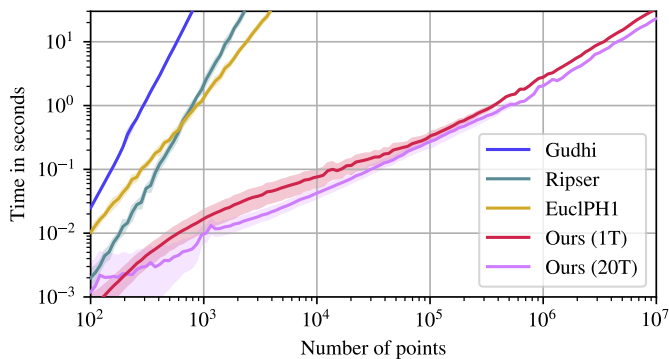


Fig. 18. Comparison of Rips persistence computation times between *Gudhi*, *Ripser*, *Euclidean PHI* and our algorithm (on a single thread, 1T, and on 20 threads, 20T), on a stress case (for *Ripser* and *Euclidean PHI*): a point cloud randomly distributed over the unit circle, with Gaussian noise ($\sigma = 0.1$).

REFERENCES

- [1] M. Moor, M. Horn, B. Rieck, and K. Borgwardt, “Topological Autoencoders,” in *International conference on machine learning*. PMLR, 2020.
- [2] K. Pearson, “On lines and planes of closest fit to systems of points in space,” *The London, Edinburgh, and Dublin philosophical magazine and journal of science*, 1901.
- [3] W. S. Torgerson, “Multidimensional Scaling: I. theory and method,” *Psychometrika*, 1952.
- [4] J. B. Tenenbaum, V. d. Silva, and J. C. Langford, “A global geometric framework for nonlinear dimensionality reduction,” *Science*, 2000.
- [5] L. Van der Maaten and G. Hinton, “Visualizing data using t-SNE,” *JMLR*, 2008.
- [6] L. McInnes, J. Healy, and J. Melville, “UMAP: Uniform Manifold Approximation and Projection for dimension reduction,” *arXiv preprint arXiv:1802.03426*, 2018.
- [7] H. Doraiswamy, J. Tierny, P. J. Silva, L. G. Nonato, and C. Silva, “TopoMap: A 0-dimensional homology preserving projection of high-dimensional data,” *IEEE TVCG*, 2020.
- [8] M. Carriere, F. Chazal, M. Glisse, Y. Ike, H. Kannan, and Y. Umeda, “Optimizing persistent homology based functions,” in *ICML*, 2021.
- [9] I. Borg and G. P., *Modern Multidimensional Scaling - Theory and Applications*. Springer Series in Statistics, 1997.
- [10] J. A. Lee and M. Verleysen, *Nonlinear Dimensionality Reduction*. Springer, 2007.
- [11] L. van der Maaten, E. Postma, and J. van den Herik, “Dimensionality reduction: A comparative review,” Tilburg University, Tech. Rep., 2007.
- [12] Z. Cunningham, J. P. Ghahramani, “Linear dimensionality reduction: Survey, insights, and generalizations,” *JMLR*, 2015.
- [13] L. G. Nonato and M. Aupetit, “Multidimensional projection for visual analytics: Linking techniques with distortions, tasks, and layout enrichment,” *IEEE TVCG*, 2019.
- [14] I. Trofimov, D. Cherniavskii, E. Tulchinskii, N. Balabin, E. Burnaev, and S. Barannikov, “Learning topology-preserving data representations,” in *ICLR*, 2023.
- [15] T. Cormen, C. E. Leiserson, R. L. Rivest, and C. Stein, *Introduction to Algorithms*. MIT Press, 2009.
- [16] G. E. Hinton and R. R. Salakhutdinov, “Reducing the dimensionality of data with neural networks,” *Science*, 2006.
- [17] S. T. Roweis and L. K. Saul, “Nonlinear dimensionality reduction by locally linear embedding,” *Science*, 2000.
- [18] V. D. Silva and J. B. Tenenbaum, “Global versus local methods in nonlinear dimensionality reduction,” in *NeurIPS*, 2003.
- [19] P. Joia, D. Coimbra, J. Cuminato, F. Paulovich, and L. Nonato, “Local affine multidimensional projection,” *IEEE TVCG*, 2011.
- [20] G. E. Hinton and S. Roweis, “Stochastic neighbor embedding,” *Advances in neural information processing systems*, 2002.
- [21] E. Amid and M. K. Warmuth, “TriMap: Large-scale dimensionality reduction using triplets,” 2022.
- [22] Y. Wang, H. Huang, C. Rudin, and Y. Shaposhnik, “Understanding how dimension reduction tools work: an empirical approach to deciphering t-SNE, UMAP, TriMap, and PaCMAP for data visualization,” *JMLR*, 2021.
- [23] C. Heine, H. Leitte, M. Hlawitschka, F. Iuricich, L. De Floriani, G. Scheuermann, H. Hagen, and C. Garth, “A survey of topology-based methods in visualization,” *CGF*, 2016.
- [24] T. Sousbie, “The persistent cosmic web and its filamentary structure: Theory and implementations,” *Royal Astronomical Society*, 2011.
- [25] N. Shivashankar, P. Pranav, V. Natarajan, R. van de Weygaert, E. P. Bos, and S. Rieder, “Felix: A topology based framework for visual exploration of cosmic filaments,” *IEEE TVCG*, 2016.
- [26] K. Anderson, J. Anderson, S. Palande, and B. Wang, “Topological data analysis of functional MRI connectivity in time and space domains,” in *MICCAI Workshop on Connectomics in NeuroImaging*, 2018.
- [27] H. A. Carr, J. Snoeyink, and M. van de Panne, “Simplifying Flexible Isosurfaces Using Local Geometric Measures,” in *IEEE VIS*, 2004.
- [28] A. Bock, H. Doraiswamy, A. Summers, and C. T. Silva, “Topoangler: Interactive topology-based extraction of fishes,” *IEEE TVCG*, 2018.
- [29] D. Guenther, R. Alvarez-Boto, J. Contreras-Garcia, J.-P. Piquemal, and J. Tierny, “Characterizing molecular interactions in chemical systems,” *IEEE TVCG*, 2014.
- [30] H. Bhatia, A. G. Gyulassy, V. Lordi, J. E. Pask, V. Pascucci, and P.-T. Bremer, “Topoms: Comprehensive topological exploration for molecular and condensed-matter systems,” *J. Comput. Chem.*, 2018.
- [31] M. Olejniczak and J. Tierny, “Topological data analysis of vortices in the magnetically-induced current density in lih molecule,” *PCCP*, 2023.
- [32] J. Kasten, J. Reininghaus, I. Hotz, and H. Hege, “Two-dimensional time-dependent vortex regions based on the acceleration magnitude,” *IEEE TVCG*, 2011.
- [33] F. Nauzeau, F. Vivodtzev, T. Bridel-Bertomeu, H. Beaugendre, and J. Tierny, “Topological analysis of ensembles of hydrodynamic turbulent flows an experimental study,” in *IEEE LDAV*, 2022.
- [34] A. Gyulassy, M. A. Duchaineau, V. Natarajan, V. Pascucci, E. Bringa, A. Higginbotham, and B. Hamann, “Topologically clean distance fields,” *IEEE TVCG*, 2007.
- [35] A. Gyulassy, A. Knoll, K. Lau, B. Wang, P. Bremer, M. Papka, L. A. Curtiss, and V. Pascucci, “Interstitial and interlayer ion diffusion geometry extraction in graphitic nanosphere battery materials,” *IEEE TVCG*, 2016.
- [36] M. Soler, M. Petitfrère, G. Darche, M. Plainchault, B. Conche, and J. Tierny, “Ranking viscous finger simulations to an acquired ground truth with topology-aware matchings,” in *IEEE LDAV*, 2019.
- [37] A. Gyulassy, P. Bremer, R. Grout, H. Kolla, J. Chen, and V. Pascucci, “Stability of dissipation elements: A case study in combustion,” *CGF*, 2014.
- [38] D. E. Laney, P. Bremer, A. Mascarenhas, P. Miller, and V. Pascucci, “Understanding the structure of the turbulent mixing layer in hydrodynamic instabilities,” *IEEE TVCG*, 2006.
- [39] H. Edelsbrunner and J. L. Harer, *Computational topology: an introduction*. AMS, 2010.
- [40] A. Zomorodian, “Computational topology,” in *Algorithms and theory of computation handbook: special topics and techniques*, 2nd ed., 2010.
- [41] F. Chazal and B. Michel, “An introduction to topological data analysis: fundamental and practical aspects for data scientists,” *Frontiers in artificial intelligence*, 2021.
- [42] G. Weber, P.-T. Bremer, and V. Pascucci, “Topological Landscapes: A Terrain Metaphor for Scientific Data,” *IEEE TVCG*, 2007.
- [43] S. Gerber, P. Bremer, V. Pascucci, and R. Whitaker, “Visual Exploration of High Dimensional Scalar Functions,” *IEEE TVCG*, 2010.

[44] S. Gerber, O. Rübel, P.-T. Bremer, V. Pascucci, and R. T. Whitaker, “Morse–Smale Regression,” *J. Comput. Graph. Stat.*, 2013.

[45] P. Oesterling, C. Heine, H. Jänicke, and G. Scheuermann, “Visual analysis of high dimensional point clouds using topological landscapes,” in *Proc. PacificVis*, 2010.

[46] P. Oesterling, G. Scheuermann, S. Teresniak, G. Heyer, S. Koch, T. Ertl, and G. H. Weber, “Two-stage framework for a topology-based projection and visualization of classified document collections,” in *Proc. IEEE VAST*, 2010.

[47] P. Oesterling, C. Heine, H. Jänicke, G. Scheuermann, and G. Heyer, “Visualization of High Dimensional Point Clouds Using their Density Distribution’s Topology,” *IEEE TVCG*, 2011.

[48] P. Oesterling, C. Heine, G. H. Weber, and G. Scheuermann, “Visualizing 3D point clouds as topological landscape profiles to guide local data analysis,” *IEEE TVCG*, 2013.

[49] L. Yan, Y. Zhao, P. Rosen, C. Scheidegger, and B. Wang, “Homology-preserving dimensionality reduction via manifold landmarking and tearing,” *CoRR*, 2018.

[50] G. Singh, F. Mémoli, and G. E. Carlsson, “Topological methods for the analysis of high dimensional data sets and 3D object recognition,” in *PBG*. Eurographics Association, 2007.

[51] G. Reeb, “Sur les points singuliers d’une forme de Pfaff complètement intégrable ou d’une fonction numérique,” *Comptes-rendus de l’Académie des Sciences*, 1946.

[52] V. Guardieiro, F. I. de Oliveira, H. Doraiswamy, L. G. Nonato, and C. Silva, “TopoMap++: A faster and more space efficient technique to compute projections with topological guarantees,” *IEEE TVCG*, 2024.

[53] S. Barannikov, I. Trofimov, N. Balabin, and E. Burnaev, “Representation topology divergence: A method for comparing neural network representations,” *arXiv preprint arXiv:2201.00058*, 2021.

[54] B. J. Nelson and Y. Luo, “Topology-preserving dimensionality reduction via interleaving optimization,” *arXiv preprint arXiv:2201.13012*, 2022.

[55] S. T. Schönenberger, A. Varava, V. Polianskii, J. J. Chung, D. Krägic, and R. Siegwart, “Witness Autoencoder: Shaping the latent space with witness complexes,” in *TDA & Beyond*, 2020.

[56] G. T. Toussaint, “The relative neighbourhood graph of a finite planar set,” *Pattern recognition*, 1980.

[57] K. J. Supowit, “The relative neighborhood graph, with an application to minimum spanning trees,” *JACM*, 1983.

[58] J. W. Jaromczyk and M. Kowaluk, “A note on relative neighborhood graphs,” in *Proceedings of the third annual symposium on Computational geometry*, 1987.

[59] A. Lingas, “A linear-time construction of the relative neighborhood graph from the Delaunay triangulation,” *Computational Geometry*, 1994.

[60] R. Urquhart, “Algorithms for computation of relative neighbourhood graph,” *Electronics Letters*, 1980.

[61] H. Edelsbrunner and T. S. Tan, “A quadratic time algorithm for the minmax length triangulation,” *SIAM Journal on Computing*, 1993.

[62] S. Barannikov, “Framed Morse complexes and its invariants.” *Adv. Soviet Math.*, 1994.

[63] P. Frosini and C. Landi, “Size theory as a topological tool for computer vision,” *Pattern Recognition and Image Analysis*, 1999.

[64] V. Robins, “Toward computing homology from finite approximations,” *Topology Proceedings*, 1999.

[65] H. Edelsbrunner, D. Letscher, and A. Zomorodian, “Topological persistence and simplification,” *DCG*, 2002.

[66] D. Cohen-Steiner, H. Edelsbrunner, and D. Morozov, “Vines and vineyards by updating persistence in linear time,” in *Proceedings of the twenty-second annual symposium on Computational geometry*, 2006.

[67] P. Skraba and K. Turner, “Wasserstein stability for persistence diagrams,” *arXiv preprint arXiv:2006.16824*, 2023.

[68] D. P. Bertsekas, “A new algorithm for the assignment problem,” *Mathematical Programming*, 1981.

[69] M. Kerber, D. Morozov, and A. Nigmetov, “Geometry helps to compare persistence diagrams,” 2017.

[70] F. Iuricich, “Persistence cycles for visual exploration of persistent homology,” *IEEE TVCG*, 2022.

[71] P. Guillou, J. Vidal, and J. Tierny, “Discrete Morse sandwich: Fast computation of persistence diagrams for scalar data—an algorithm and a benchmark,” *IEEE TVCG*, 2023.

[72] U. Bauer, “Ripser: efficient computation of Vietoris–Rips persistence barcodes,” *Journal of Applied and Computational Topology*, 2021.

[73] C. Maria, J.-D. Boissonnat, M. Glisse, and M. Yvinec, “The Gudhi library: Simplicial complexes and persistent homology,” in *ICMS*, 2014.

[74] U. Bauer, M. Kerber, J. Reininghaus, and H. Wagner, “PHAT – Persistent homology algorithms toolbox,” *Journal of symbolic computation*, 2017.

[75] P. Skraba, G. Thoppe, and D. Yogeshwaran, “Randomly weighted d –complexes: Minimal spanning acycles and persistence diagrams,” *arXiv preprint arXiv:1701.00239*, 2017.

[76] M. A. Koyama, V. Robins, K. Turner, and F. Memoli, “Reduced Vietoris–Rips complexes: New methods to compute Vietoris–Rips persistent homology,” *arXiv preprint arXiv:2307.16333*, 2023.

[77] A. Fabri and S. Pion, “CGAL: the Computational Geometry Algorithms Library,” in *Proceedings of the 17th ACM SIGSPATIAL International Conference on Advances in Geographic Information Systems*, 2009.

[78] A. Paszke, S. Gross, F. Massa, A. Lerer, J. Bradbury, G. Chanan, T. Killeen, Z. Lin, N. Gimelshein, L. Antiga, A. Desmaison, A. Kopf, E. Z. Yang, Z. DeVito, M. Raison, A. Tejani, S. Chilamkurthy, B. Steiner, L. Fang, J. Bai, and S. Chintala, “PyTorch: An Imperative Style, High-Performance Deep Learning Library,” in *NeurIPS*, 2019.

[79] J. Tierny, G. Favelier, J. A. Levine, C. Gueunet, and M. Michaux, “The Topology ToolKit,” *IEEE TVCG*, 2017.

[80] T. B. Masood, J. Budin, M. Falk, G. Favelier, C. Garth, C. Gueunet, P. Guillou, L. Hofmann, P. Hristov, A. Kamakshidasan *et al.*, “An overview of the Topology ToolKit,” *Topological Methods in Data Analysis and Visualization VI: Theory, Applications, and Software*, 2021.

[81] D. P. Kingma and J. Ba, “Adam: A method for stochastic optimization,” *arXiv preprint arXiv:1412.6980*, 2017.

[82] S. A. Nene, S. K. Nayar, and H. Murase, “Columbia Object Image Library (COIL-20),” 1996.

[83] B. Wang, B. Summa, V. Pascucci, and M. Vejdemo-Johansson, “Branching and circular features in high dimensional data,” *IEEE TVCG*, 2011.

[84] “Carnegie Mellon University - CMU Graphics Lab - Motion capture library.” [Online]. Available: <http://mocap.cs.cmu.edu/>

[85] W. Saelens, R. Cannoodt, H. Todorov, and Y. Saeys, “A comparison of single-cell trajectory inference methods,” *Nature biotechnology*, 2019.

[86] R. Cannoodt, W. Saelens, H. Todorov, and Y. Saeys, “Single-cell -omics datasets containing a trajectory,” 2018. [Online]. Available: <https://zenodo.org/records/1443566>

[87] F. Pedregosa, G. Varoquaux, A. Gramfort, V. Michel, B. Thirion, O. Grisel, M. Blondel, P. Prettenhofer, R. Weiss, V. Dubourg *et al.*, “Scikit-learn: Machine learning in python,” *JMLR*, 2011.

[88] J. A. Lee and M. Verleysen, “Quality assessment of dimensionality reduction: Rank-based criteria,” *Neurocomputing*, 2009.

[89] J. Venna and S. Kaski, “Local multidimensional scaling,” *Neural Networks*, 2006.

APPENDIX A ADDITIONAL BACKGROUND

A. Homology

Homology groups, introduced by Henri Poincaré in the early 20th century in his *Analysis Situs*, are algebraic constructions that describe "holes" in a topological space. Here, we provide a brief summary of the notions used to define them.

Let \mathcal{K} be a simplicial complex. A k -chain c is a formal sum of k -simplices with *modulo 2* coefficients³: $c = \sum \alpha_i \sigma_i$ with $\alpha_i \in \mathbb{Z}/2\mathbb{Z}$. Two k -chains can be summed simplex by simplex, which permits to define the group of k -chains, noted $\mathcal{C}_k(\mathcal{K})$. The *boundary* of a k -simplex is the sum of its $(k-1)$ -dimensional faces, i.e. more formally, if $\sigma = (v_0, \dots, v_k)$, then its boundary is

$$\partial_k \sigma = \sum_{i=0}^k (v_0, \dots, \hat{v}_i, \dots, v_k)$$

where the hat means that v_i is omitted. Then the boundary of a k -chain c is defined as the modulo 2 sum of the boundaries of its simplices, i.e. $\partial_k c = \sum \alpha_i \partial_k \sigma_i$. This defines the k -th *boundary map* ∂_k , which is a morphism $\partial_k : \mathcal{C}_k(\mathcal{K}) \rightarrow \mathcal{C}_{k-1}(\mathcal{K})$.

A k -cycle is a k -chain whose boundary is 0. The group of k -cycles is noted $\mathcal{Z}_k(\mathcal{K}) = \ker \partial_k$. A k -boundary is a k -chain which is the boundary of some $(k+1)$ -chain. The group of k -boundaries is noted $\mathcal{B}_k(\mathcal{K}) = \text{Im } \partial_{k+1}$. The fundamental lemma of homology states that $\partial_{k-1} \circ \partial_k = 0$, i.e., that the boundary of a boundary is always an empty chain. In particular this implies the inclusions $\mathcal{B}_k(\mathcal{K}) \subseteq \mathcal{Z}_k(\mathcal{K}) \subseteq \mathcal{C}_k(\mathcal{K})$.

Two k -cycles $a, b \in \mathcal{Z}_k(\mathcal{K})$ are *homologous* whenever $a = b + \partial c$ for some $c \in \mathcal{C}_{k+1}(\mathcal{K})$. The set of the equivalence classes for this relation forms the k -th homology group of \mathcal{K} : $\mathcal{H}_k(\mathcal{K}) = \mathcal{Z}_k(\mathcal{K})/\mathcal{B}_k(\mathcal{K})$. Its rank, i.e. the maximal number of linearly independent classes (called *generators*), is called the k -th *Betti number* of \mathcal{K} : $\beta_k(\mathcal{K}) = \text{rank } \mathcal{H}_k(\mathcal{K}) = \log_2(|\mathcal{H}_k(\mathcal{K})|)$. The Betti numbers can be easily interpreted geometrically for small values of k : for a simplicial complex \mathcal{K} embedded in \mathbb{R}^3 , $\beta_0(\mathcal{K})$ is the number of connected components, $\beta_1(\mathcal{K})$ is the number of cycles, and $\beta_2(\mathcal{K})$ is the number of voids.

B. Minmax length triangulations

In this section, we give more details on the computation of minmax length (MML) triangulations, that are all taken from [61]. General position is supposed, i.e., no two edges are equally long. A *2-edge* is an edge whose right and left lenses are both non-empty. Conversely, a *1-edge* is an edge such that one of its half-lens is empty but not the other one. By definition, 1- and 2-edges are not RNG edges. Note that every triangulation of an RNG polygon has a 2-edge (its longest edge is always a 2-edge).

An *expandable 2-edge* is a 2-edge $e = pq$ for which there exists $x \in \text{LeftLens}(e)$ and $y \in \text{RightLens}(e)$ such that the edges px, xq, qy, yp are either RNG edges, or 1-edges with

³The coefficients can be chosen in another field or ring (which yields different homology groups), but $\mathbb{Z}/2\mathbb{Z}$ is the most common choice.

an empty right lens (see Fig. 12). Expandability is a property that somehow allows an edge to be the longest edge of a triangulation. Indeed, let e be an expandable 2-edge inside an RNG-polygon Π . Then it is possible to construct by recurrence a triangulation of Π such that the only 2-edge – and thus longest edge – in that triangulation is e itself.

Besides, the *2-edge lemma* (Sec. 5.3 of [61]) states that there exists a MML triangulation of Π that contains an expandable 2-edge. Therefore, to find a MML triangulation of an RNG-polygon, it suffices to find the shortest expandable 2-edge e , which is the longest edge of any MML-triangulation. This is the only information we use in our application. However, if a complete MML triangulation is wanted, $e = pq$ has to be found together with x and y defined as above. Then, the incomplete polygons defined by px, xq, qy, yp have to be triangulated (Sec. 5.1 of [61]).

APPENDIX B

RAW DATA FOR FIG. 8

The point clouds $X \subset \mathbb{R}^3$ and $Z \subset \mathbb{R}^2$ used in the counter-example depicted in Fig. 8 are given by the following coordinates:

$$X = \begin{bmatrix} 1 & 0 & 0 \\ 0.5 & 0.866 & 0 \\ -0.48 & 0.667 & 0 \\ -0.73 & -0.199 & 0.433 \\ -0.48 & -1.065 & 0 \\ 0.5 & -0.866 & 0 \end{bmatrix} \quad Z = \begin{bmatrix} 1 & 0 \\ 0.5 & 0.866 \\ -0.48 & 0.667 \\ -0.98 & -0.199 \\ -0.48 & -1.065 \\ 0.5 & -0.866 \end{bmatrix}.$$

APPENDIX C

DETAILED PROOF FOR LEM. 3

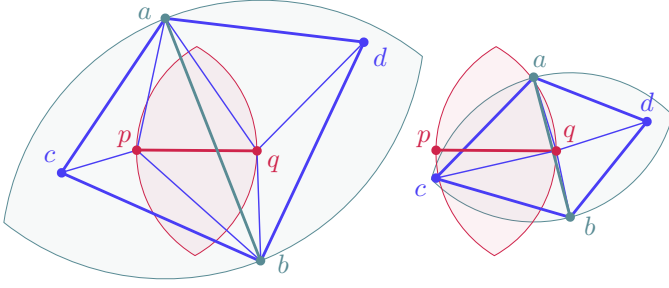
In this section, we restate Lem. 3 and then prove it.

Lemma 3. *In the plane, an edge that intersects an RNG edge kills no PH¹ class of positive persistence.*

Proof. Let ab be an edge that intersects an RNG edge pq . Suppose that ab kills a PH¹ class γ of positive persistence. Then ab is the longest edge of two triangles abc and abd , where $acbd$ is a representative 1-cycle of γ , and such that c and d are on both sides of $\text{Lens}(a, b)$ (see Fig. 10). Thus, by definition, all distances $|ac|, |bc|, |ad|$ and $|bd|$ are $< |ab|$. Moreover, wlog, we can suppose that c and p , and d and q , are in the same half-space delimited by the line (ab) .

We first show that at least p or q belongs to $\text{Lens}(a, b)$. Suppose that both p and q are outside $\text{Lens}(a, b)$. Then, both pq and ab are in $\text{RNG}(\{a, b, p, q\}) \subset \text{DEL}(\{a, b, p, q\})$. This implies that this Delaunay triangulation features two edges that intersect, which is impossible. Therefore, we have two remaining cases:

- 1) Both p and $q \in \text{Lens}(a, b)$ (Fig. 10, left). In this case, the lengths $|ap|, |bp|, |aq|, |bq|$ are all $< |ab|$. In addition, since $a \notin \text{Lens}(p, q)$, either $|ap| \geq |pq|$ or $|aq| \geq |pq|$, which implies $|pq| < |ab|$ with the above inequalities. Finally, c and p , and d and q , are in the same half-lens of $\text{Lens}(a, b)$, hence $|cp| < |ab|$ and $|dq| < |ab|$. Therefore, the 2-chain $acp + bcp + apq + bpq + adq + bdq$, whose boundary is $acbd$, contains only triangles of diameter $< |ab|$.



2) $p \notin \text{Lens}(a, b)$ and $q \in \text{Lens}(a, b)$ (Fig. 10, right; the symmetric case is handled similarly). In this case, $|aq| < |ab|$ and $|bq| < |ab|$. In addition, like in the previous case, d and q are in the same half-lens of $\text{Lens}(a, b)$, hence $|dq| < |ab|$. The last inequality to show is $|cq| < |ab|$.

First, we show that $|ap| \geq |pq|$ and $|bp| \geq |pq|$ (i.e., we are in a configuration similar to the one depicted Fig. 10, right).

To prove the first inequality, suppose by contradiction that $|ap| < |pq|$ (we can do a similar reasoning to prove $|bp| \geq |pq|$). Then, as $a \notin \text{Lens}(p, q)$, we have $|aq| \geq |pq|$, hence $|ap| < |pq| \leq |aq| < |ab|$. Therefore, as by hypothesis $p \notin \text{Lens}(a, b)$, we have $|bp| \geq |ab|$. Now, remind that ab intersects pq by hypothesis. Because of that, due to triangular inequalities, the sum of two opposite edges of the quadrilateral $apbq$ is smaller than the sum of the two diagonals, i.e., $|aq| + |bp| < |ab| + |pq|$. This gives $|bp| < |ab| + (|pq| - |aq|) \leq |ab|$ (because $|pq| \leq |aq|$), hence a contradiction.

Now, notice that as $p \notin \text{Lens}(a, b)$, either ac or bc intersects pq . Indeed, if not, p lies inside the interior of the triangle abc , which is included in $\text{Lens}(a, b)$. Suppose that ac intersects pq (the other case is handled similarly). Because of that, once again due to triangular inequalities, the sum of two opposite edges of the quadrilateral $cqap$ is smaller than the sum of the two diagonals: $|cq| + |ap| < |ac| + |pq|$, hence $|cq| < |ac| + (|pq| - |ap|) < |ab|$ (because $|ac| < |ab|$ and $|ap| \geq |pq|$).

Therefore, the 2-chain $acq + bcq + adq + bdq$, whose boundary is $acbd$, contains only triangles of diameter $< |ab|$.

In both cases, there always exists a 2-chain of boundary $acbd$, that contains only triangles of diameter $< |ab|$. Hence, the PH^1 class γ is killed before the value $|ab|$, thus not by ab . \square

APPENDIX D

ADDITIONAL QUANTITATIVE ANALYSIS

Fig. 19 shows the values of PH -related metrics (PDW^0 and PDW^1) and some common DR indicators for the examples presented in the paper. These additional indicators measure the preservation of global distances (pairwise distances-based and triplets-based indicators) and the preservation of local distances (rank-based indicators).

A. Description of the indicators

a) *Pairwise distances-based indicators:* In addition to the metric distortion \mathfrak{D} , one can measure the linear correlation $\text{LC} \in [-1, 1]$ between the pairwise distances in X and in

Z . Having $\text{LC} = 1$ means that these pairwise distances are perfectly correlated in high and low dimension.

b) *Triplets-based indicator:* The *triplet accuracy* $\text{TA} \in [0, 1]$ is the proportion of triangles whose three edges have the same relative order (in terms of length) both in high and low dimension [22]. It measures to some extent the preservation of the global structure of X , which is preserved when $\text{TA} = 1$.

c) *Rank-based indicators:* The rank of a point X_i relative to another point X_j is the integer $\rho_{ij} \in \mathbb{N}$ such that X_j is the ρ_{ij} -th nearest neighbor of X_i . There exists indicators based on these ranks [88], [89] that measure the preservation of the nearest neighbors. In particular, the *trustworthiness* ($\text{Trust} \in [0, 1]$) is penalized when a high rank ρ_{ij} in the input becomes low in the representation, i.e., when faraway points in high-dimension become neighbors in low-dimension. On the contrary, the *continuity* ($\text{Cont} \in [0, 1]$) is penalized when a low rank ρ_{ij} in the input becomes high in the representation, i.e., when neighbors in high-dimension are projected to faraway points in low-dimension. These indicators are computed for a number K of nearest neighbors (in our experiments, $K = 10$).

B. Observations

TopoMap has the best results for PDW^0 , which is expected since it preserves by design exactly PH^0 . Although in theory this quantity should be exactly 0, the approximation performed by the auction algorithm when estimating the Wasserstein distance (to compute PDW^0) makes it slightly positive. Our approach (TopoAE++) has competitive results for this metric as well, which was expected since, as TopoAE, it constrains the preservation of PH^0 in the sense of Lem. 1.

Global indicators, namely the metric distortion \mathfrak{D} , the linear correlation LC between pairwise distances and the triplet accuracy TA , are best preserved by global methods, i.e., PCA and MDS. Our approach (TopoAE++) presents competitive results for these indicators when comparing to other locally topology-aware methods, while it clearly outperforms globally topology-aware methods.

Finally, TopoAE++ also presents good results for neighborhood quality indicators (Trust and Cont). Indeed, in our datasets, the correct embedding of the input cycle(s) favors the preservation of the neighborhood. More precisely, a self-intersection in the projection of an input cycle penalizes the trustworthiness (since faraway vertices would be projected as neighbors near this intersection), while a broken input cycle penalizes the continuity (since two neighbors in the input generator would be embedded faraway in low-dimension).

APPENDIX E

HYPERPARAMETERS

We provide a study of the hyperparameters describing the autoencoder's architecture (size of the hidden layers, Fig. 20) and its optimization (learning rate and weight applied to the topological regularization term, Fig. 21), on COIL-20-1 and SingleCell datasets. Except for very small networks (8-8 or 16-16), the size of the hidden layers has little impact on the performance of the autoencoder. The 128-32 choice gives an acceptable compromise for our datasets. We found

Dataset	Indicator	Global methods		Locally topology-aware methods			Globally topology-aware methods			
		PCA [2]	MDS [3]	Isomap [4]	t-SNE [5]	UMAP [6]	TopoMap [7]	TopoAE [1]	TopoAE+ \mathcal{W}^1 [8]	TopoAE++
3Clusters	PD \mathcal{W}^0	2.0e+01	1.5e+01	2.6e+01	6.7e+02	2.1e+02	4.2e-04	2.0e+01	1.2e+01	1.0e+01
	PD \mathcal{W}^1	4.5e-01	5.0e-01	4.7e-01	2.3e+01	7.2e-01	4.3e+00	5.8e-01	1.1e-01	4.4e-01
	\mathfrak{D}	<u>2.7e-01</u>	<u>4.1e-01</u>	1.1e+00	3.5e+01	8.5e+00	7.0e+00	1.3e+00	1.5e+00	6.4e-01
	LC	1.00	<u>0.99</u>	0.98	0.85	0.89	0.86	0.95	0.93	0.97
	TA	0.89	<u>0.88</u>	0.72	0.38	0.42	0.48	0.70	0.66	0.78
	Trust	0.93	0.94	0.92	0.99	<u>0.98</u>	0.96	0.97	0.97	0.96
	Cont	0.99	0.98	0.98	0.98	0.98	0.92	0.98	0.97	0.98
Twist	PD \mathcal{W}^0	1.1e-01	1.3e-01	4.5e-01	2.9e+00	6.6e-01	7.5e-06	8.6e-02	2.8e-02	<u>5.2e-03</u>
	PD \mathcal{W}^1	1.1e+00	2.2e-01	1.9e+01	3.3e+00	1.5e+01	1.8e-01	1.6e-01	1.8e-05	<u>1.7e-03</u>
	\mathfrak{D}	<u>2.2e-01</u>	2.1e-01	2.4e+00	3.9e+00	2.8e+00	8.2e-01	3.8e-01	7.3e-01	7.8e-01
	LC	0.99	<u>0.99</u>	0.86	0.99	0.58	0.86	0.98	0.99	0.99
	TA	0.91	<u>0.89</u>	0.63	0.87	0.42	0.64	0.85	0.87	0.88
	Trust	0.98	0.99	1.00	0.99	1.00	0.99	0.99	0.96	1.00
	Cont	0.99	0.99	1.00	0.99	1.00	0.98	0.99	0.98	1.00
K_4	PD \mathcal{W}^0	1.2e-01	6.9e-02	1.1e-01	3.0e+01	2.0e+01	2.3e-07	1.9e-01	7.8e-02	<u>5.8e-02</u>
	PD \mathcal{W}^1	2.7e-01	2.8e-01	3.8e-01	4.7e+01	3.9e-01	1.4e-01	6.5e-02	7.9e-04	<u>2.4e-02</u>
	\mathfrak{D}	<u>2.7e-01</u>	1.8e-01	5.1e-01	1.6e+01	9.1e+00	5.7e-01	1.0e+00	6.8e-01	<u>3.4e-01</u>
	LC	0.83	<u>0.89</u>	0.65	0.66	0.53	0.57	0.75	0.68	0.77
	TA	0.61	<u>0.63</u>	0.39	0.48	0.34	0.38	0.51	0.47	0.56
	Trust	0.97	0.98	0.95	1.00	1.00	0.99	0.98	0.98	1.00
	Cont	1.00	1.00	1.00	0.99	0.99	0.98	0.99	0.99	1.00
K_5	PD \mathcal{W}^0	2.7e-01	1.5e-01	1.8e-01	9.3e+01	1.8e+01	7.3e-07	2.2e-01	1.3e-01	<u>9.0e-02</u>
	PD \mathcal{W}^1	2.8e-01	3.5e-01	1.3e-01	4.7e+01	9.7e-01	4.8e-01	1.6e-01	2.2e-03	<u>8.0e-02</u>
	\mathfrak{D}	<u>3.1e-01</u>	2.4e-01	4.7e-01	2.1e+01	9.8e+00	1.2e+00	9.2e-01	8.6e-01	<u>3.4e-01</u>
	LC	0.81	<u>0.86</u>	0.67	0.76	0.58	0.41	0.73	0.72	0.81
	TA	0.63	<u>0.61</u>	0.43	0.55	0.41	0.33	0.50	0.50	0.57
	Trust	0.93	0.97	0.96	1.00	<u>1.00</u>	0.99	0.99	0.97	1.00
	Cont	0.99	0.99	1.00	0.99	0.98	0.97	0.99	0.99	1.00
COIL-20-1	PD \mathcal{W}^0	1.2e+02	8.1e+01	3.0e+00	1.5e+02	1.5e+02	2.3e-06	1.9e+00	4.5e+00	<u>1.2e+00</u>
	PD \mathcal{W}^1	1.2e+01	1.0e+01	6.0e+02	1.3e+01	1.2e+01	2.7e+01	7.5e+00	<u>9.1e-02</u>	1.6e-02
	\mathfrak{D}	<u>2.9e+00</u>	2.0e+00	2.1e+01	4.9e+00	6.2e+00	7.2e+00	8.2e+00	6.7e+00	<u>1.9e+01</u>
	LC	0.94	<u>0.93</u>	0.83	0.88	0.85	0.74	0.81	0.62	0.88
	TA	0.81	<u>0.74</u>	0.47	<u>0.77</u>	0.65	0.44	0.56	0.38	0.73
	Trust	0.97	0.97	1.00	1.00	0.99	0.92	0.96	0.91	0.99
	Cont	0.96	0.97	0.98	1.00	0.99	0.96	0.97	0.94	0.99
MoCap	PD \mathcal{W}^0	4.3e+03	2.2e+03	3.9e+02	6.8e+03	6.8e+03	2.4e-03	1.6e+03	7.9e+02	<u>1.9e+03</u>
	PD \mathcal{W}^1	2.1e+03	1.9e+03	1.0e+04	1.6e+03	1.5e+03	2.1e+03	1.2e+03	9.4e+00	<u>1.2e+01</u>
	\mathfrak{D}	<u>2.4e+01</u>	1.7e+01	1.3e+02	9.9e+01	1.0e+02	8.5e+01	2.6e+01	5.6e+01	<u>2.9e+01</u>
	LC	0.94	<u>0.95</u>	0.67	0.90	0.47	0.43	0.89	0.61	0.83
	TA	0.72	<u>0.73</u>	0.53	0.64	0.34	0.35	0.68	0.42	0.59
	Trust	0.98	0.98	<u>1.00</u>	1.00	1.00	0.97	0.98	0.93	1.00
	Cont	0.98	0.99	1.00	1.00	0.99	0.98	0.99	0.98	1.00
SingleCell	PD \mathcal{W}^0	4.6e+05	4.6e+05	3.5e+05	4.6e+05	4.6e+05	1.2e-01	4.6e+05	<u>1.6e+05</u>	<u>3.8e+05</u>
	PD \mathcal{W}^1	3.0e+03	3.1e+03	1.8e+03	1.8e+03	1.8e+03	2.8e+04	1.8e+03	6.4e+02	<u>8.6e+02</u>
	\mathfrak{D}	<u>3.1e+01</u>	2.3e+01	4.8e+02	9.6e+01	1.0e+02	1.2e+03	9.8e+01	3.2e+02	<u>1.5e+02</u>
	LC	0.99	<u>0.98</u>	0.98	0.88	0.81	0.62	0.72	0.74	0.85
	TA	0.94	<u>0.86</u>	0.84	0.68	0.54	0.40	0.55	0.52	0.61
	Trust	0.99	0.99	0.99	0.99	0.99	0.96	0.97	0.96	0.97
	Cont	0.99	0.99	0.99	0.99	0.99	0.95	0.94	0.96	0.96

Fig. 19. PH-based metrics and other common indicators used in DR (see Sec. D for a description). The best value (before rounding) for an indicator is written in bold, the second best (before rounding) is underlined.

that a learning rate of 10^{-2} gives good results for our datasets. Finally, the weight applied on $\mathcal{L}_{\text{CD}}^1$ has to be chosen according to the dataset as it scales with its size. For instance, we used 10^{-2} for COIL-20-1 and 10^{-4} for SingleCell.

APPENDIX F FAILURES CASES

We show in Fig. 22 a histogram of the final values of PDW^0 , PDW^1 and $\mathcal{L}_{\text{CD}}^1$ computed for 1000 runs of TopoAE++ on COIL-20-1. For this dataset, the distributions of PDW^1 and $\mathcal{L}_{\text{CD}}^1$ are typically bimodal (this is also visible in Fig. 20, top line). This reflects the existence of *successful* runs (no input generator self-crossing, see left example) and *unsuccessful* runs (trapped in a bad local minima featuring an input self-crossing, see right example). Even though we have currently mitigated this issue by keeping the best of

several runs, this could be handled in future work with more elaborated initializations and by penalizing input generators' self-crossings during optimization. Finally, note that this phenomenon does not appear with all datasets (e.g., with SingleCell, see Fig. 20, bottom line, where distributions are not bimodal).

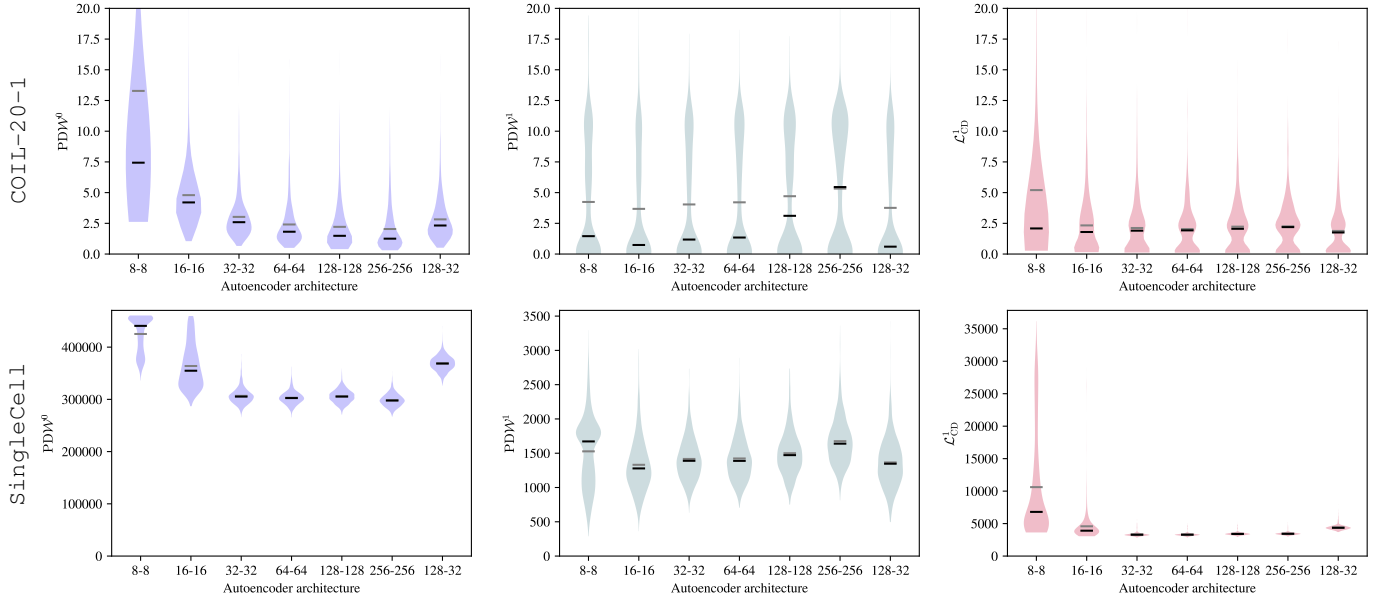


Fig. 20. Violin plots of the distribution of the final value of $\mathcal{L}_{\text{CD}}^1$ according to the size of the autoencoder's layers, computed for 1000 runs of our method on COIL-20-1 for the top line and SingleCell for the bottom line. We only consider here encoders with two fully connected hidden layers, whose size is indicated by the two numbers (the decoder is symmetrical). The mean value is shown in gray and the median in black. The rightmost violins of each chart in the top line correspond to the histogram in Fig. 22.

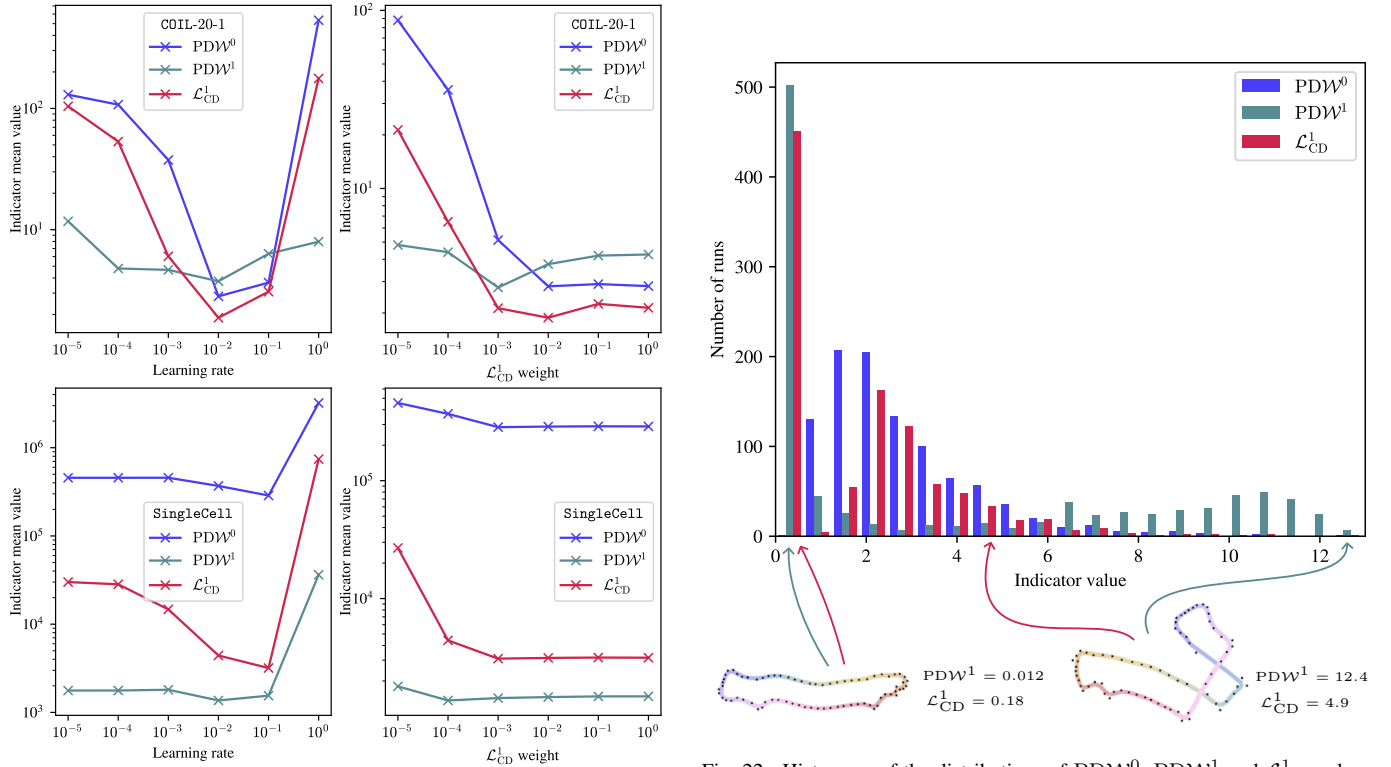


Fig. 21. Mean final values of PDW^0 (dark blue), PDW^1 (teal) and $\mathcal{L}_{\text{CD}}^1$ (red) for varying learning rates (left) and varying weights applied to the $\mathcal{L}_{\text{CD}}^1$ regularisation term, computed for 1000 runs of our method on COIL-20-1 (top line) and SingleCell (bottom line).

Fig. 22. Histogram of the distributions of PDW^0 , PDW^1 and $\mathcal{L}_{\text{CD}}^1$ values after the optimization for 1000 runs of TopoAE++ on COIL-20-1. Two examples of results are shown at the bottom: one successful on the left, the other unsuccessful on the right.